

TreeLoc++: Robust 6-DoF LiDAR Localization in Forests with a Compact Digital Forest Inventory

Minwoo Jung¹, Dongjae Lee¹, Nived Chebrolu², Haedam Oh², Maurice Fallon² and Ayoung Kim¹

¹Department of Mechanical Engineering, Seoul National University, Seoul, South Korea

²Oxford Robotics Institute, Department of Engineering Science, University of Oxford, Oxford, UK

Corresponding author: Ayoung Kim (email: ayoungk@snu.ac.kr).

This work was supported by the National Research Foundation of Korea (NRF) grant funded by the Korea government (MSIT) (No. RS-2024-00461409); the Horizon Europe project DigiForest (101070405); and EPSRC Project Mobile Robotic Inspector (EP/Z531212/1).

ABSTRACT Reliable localization is essential for sustainable forest management, as it allows robots or sensor systems to revisit and monitor the status of individual trees over long periods. In modern forestry, this management is structured around Digital Forest Inventories (DFIs), which encode stems using compact geometric attributes rather than raw data. Despite their central role, DFIs have been overlooked in localization research, and most methods still rely on dense gigabyte-sized point clouds that are costly to store and maintain. To improve upon this, we propose TreeLoc++, a global localization framework that operates directly on DFIs as a discriminative representation, eliminating the need to use the raw point clouds. TreeLoc++ substantially strengthens the existing TreeLoc framework by reducing false matches in structurally ambiguous forests and improving the reliability of full 6-DoF pose estimation. Building upon TreeLoc, it augments coarse retrieval with a pairwise distance histogram that encodes local tree-layout context, subsequently refining candidates via DBH-based filtering and yaw-consistent inlier selection to further reduce mismatches. Furthermore, a constrained optimization leveraging tree geometry jointly estimates roll, pitch, and height, enhancing pose stability and enabling accurate localization without reliance on dense 3D point cloud data. Evaluations on 27 sequences recorded in forests across three datasets and four countries show that TreeLoc++ achieves precise localization with centimeter-level accuracy. We further demonstrate robustness to long-term change by localizing data recorded in 2025 against inventories built from 2023 data, spanning a two-year interval. The system represents 15 sessions spanning 7.98 km of trajectories using only 250 KB of map data and outperforms both hand-crafted and learning-based baselines that rely on dense point cloud maps. This demonstrates the scalability of TreeLoc++ for long-term deployment. Code and datasets will be released to support future research.

INDEX TERMS Environmental Monitoring, Global Localization, Place Recognition, Pose Estimation

I. Introduction

Reliable and accurate localization is essential in forestry and environmental monitoring, where systems operate in complex under-canopy environments [1–3]. Localization enables key long-term tasks such as repeated site access, consistent map maintenance under dynamic canopy conditions, and digital inventory updates for sustainable forest management [4–6]. For practical deployment, localization systems must be robust to challenges specific to forests

such as structural repetition and seasonal variation, provide centimeter-level accuracy, and rely on input representations that minimize storage and computational overhead in long-term, resource-constrained missions [7, 8].

While satellite-based localization systems such as GNSS are widely used in outdoor environments, they struggle in forests due to signal degradation under dense canopies [9]. Even high-precision RTK services often fail to maintain consistent performance [10], resulting in meter-level errors,

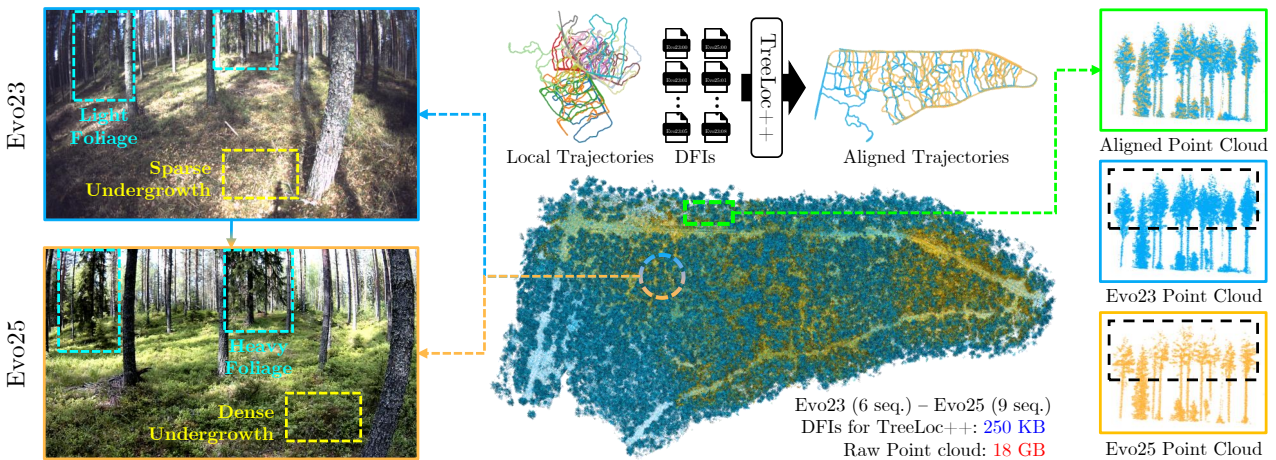


FIGURE 1: (Left) Images captured from the same location in the Evo forest two years apart, showing vegetation growth (yellow) and denser foliage (cyan), which amplifies perceptual aliasing. (Right) TreeLoc++ achieves accurate multi-session alignment using only lightweight DFIs by leveraging tree attributes, avoiding raw point clouds that can vary across sessions due to different LiDAR sensors (black).

which are insufficient for tasks requiring tree-level correspondence such as growth estimation [11]. These limitations underscore the need for onboard, geometry-based alternatives that do not rely on external positioning infrastructure; LiDAR is a promising solution due to its ability to capture precise 3D geometric information [12, 13].

The standard LiDAR-based global localization pipeline [1] typically involves place recognition for candidate retrieval [14–16] followed by pose estimation through descriptor matching [17–19] or scan registration [20–22]. While effective in structured environments, these methods incur high memory usage due to dense point cloud storage while localization performance degrades in forests, where geometrically similar scenes and seasonal variation cause perceptual aliasing [23]. This leads to more frequent retrieval errors and unstable pose estimates.

To mitigate reliance on dense point clouds and reduced discriminative power in forests, recent research has proposed compact, high-level representations as alternatives to raw point clouds [24, 25]. Segmentation-based methods reduce storage by clustering geometrically or semantically similar points, but their discriminative power remains limited in forests due to low semantic diversity, where only a few semantic categories recur [26]. Other methods such as ESM [27] and NSM [28] extract descriptors from individual tree instances, but still rely on point clouds and overlook inter-tree relationships, making them prone to perceptual aliasing in environments where tree geometries are indistinguishable. These limitations motivate the use of more compact and interpretable representations that are better suited to the structural characteristics of forest environments.

A more compact alternative would be to use a Digital Forest Inventory (DFI) directly for localization. A DFI represents each tree by attributes such as stem axis and diameter at breast height (DBH) without requiring any raw point clouds. TreeLoc [29] introduced a DFI-based framework that leverages inter-tree spatial relationships for matching. While

efficient, it remains sensitive to structural aliasing, where locally similar tree layouts repeat across different parts of the forest, leading to incorrect matches and localization failures.

To overcome these limitations, we propose TreeLoc++, a forest-specific localization system that builds on TreeLoc to address structural ambiguity and false correspondence matches, improving candidate retrieval and enabling reliable 6-DoF pose estimation. TreeLoc++ enhances the original coarse-to-fine framework with components that improve robustness and efficiency. It augments the Tree Distribution Histogram (TDH) introduced in TreeLoc, a histogram-based descriptor encoding individual tree attributes, with a novel Pairwise Distance Histogram (PDH) that injects pairwise geometric context into coarse retrieval to improve accuracy. In the refinement stage, DBH-based filtering eliminates attribute-inconsistent correspondences, and yaw voting using matched triangle relationships rejects pose-inconsistent matches and suppresses outliers caused by hash collisions. These components reduce false positives from structural aliasing and preserve pose-consistent inliers, resulting in robust candidate correspondences for subsequent verification.

Given reliable candidates, TreeLoc++ performs geometric verification and fine-grained pose estimation through two complementary strategies. It evaluates alignment quality using an overlap score that incorporates a spatial proximity prior and discourages associations between geometrically similar but spatially distant scenes. This design reflects the fact that stem reconstruction quality is viewpoint-dependent, and shared trees between distant scenes are often observed under different conditions, leading to inconsistent geometry and increased mismatches. Additionally, TreeLoc++ applies a constrained 6-DoF optimization that jointly estimates roll, pitch, and height by enforcing geometric consistency among matched tree geometry, in contrast to prior methods that estimate these components independently.

As shown in Fig. 1, TreeLoc++ offers a lightweight and scalable alternative to conventional point cloud-based local-

ization systems. By using only a compact DFI as its prior map, it supports efficient multi-session alignment without retaining or revisiting raw scans. Its stem-based representation also enables accurate and seasonally robust localization. This lightweight and stable localization pipeline supports continuous DFI updates across sessions, enabling long-term forest monitoring and management. Our contributions are summarized as follows:

- An advanced global localization framework for forests that resolves geometric ambiguity in tree-based configurations. Our framework also improves 6-DoF pose estimation by leveraging tree geometry and optimizing roll, pitch, and height simultaneously, enabling accurate localization in complex under-canopy conditions.
- A retrieval pipeline combining TDH and PDH, which jointly encodes individual tree attributes and inter-tree connectivity. This combination strengthens coarse retrieval, ensuring high recall and increasing the fraction of true positives among the top-ranked candidates.
- Robust outlier rejection through DBH-based filtering and yaw-consistent inlier voting. These methods reduce ambiguous matches caused by hash collisions, enabling more consistent candidate retrievals for precise place recognition and pose estimation, particularly in scenarios with repeated or symmetric tree layouts.
- Practical applicability across diverse localization scenarios such as inter-session localization, global map alignment, and continuous DFI updates. This is enabled by an overlap score that identifies true positives across sessions without environment-specific tuning, ensuring reliable performance in real-world deployments.
- Extensive benchmarking on three datasets with structural diversity and seasonal variations shows that TreeLoc++ consistently outperforms existing methods. Compared to the learning-based method LoGG3D-Net, it improves place recognition on E_{VO} from 0.521 to 0.940 in Recall@1 and reduces pose estimation error from decimeter-level to centimeter-level, while requiring only kilobytes of map storage with query times under 10 ms.

II. Related Work

A. Digital Forest Inventories from Tree Segmentation

LiDAR plays a central role in forestry, supporting biodiversity monitoring, biomass estimation, and sustainable forest management [6, 30]. Both static terrestrial LiDAR systems and mobile LiDAR platforms provide high-resolution 3D data for detailed forest analysis [5]. A key application is individual tree segmentation [31–35], addressed through traditional clustering and deep learning methods such as PointNet++ [36] and RandLA-Net [37]. Public forest datasets [23, 26, 38, 39] have further accelerated research progress.

From segmented point clouds, tree attributes such as height, crown structure, stem position, orientation, and DBH can be extracted [35, 40]. These parameters form the basis of

the DFI, a compact, point cloud-independent representation that supports applications in precision forestry and long-term monitoring. RealtimeTrees [35] introduced a learning-free pipeline for real-time DFI construction for mobile platforms, eliminating the need for post-processing. While DFI construction has become efficient, applying DFIs across multiple sessions introduces new challenges. Effective forest monitoring requires not only generating local inventories, but also localizing new observations against prior maps to detect revisits and to maintain correspondence between individual trees observed at different times. These capabilities are critical for enabling inventory updates, long-term monitoring, and consistent map integration, highlighting the need for robust global localization in forest environments [9, 41].

B. LiDAR-based Global Localization

Accurate forest localization is challenging due to GNSS degradation under dense canopies, making LiDAR-based global localization a viable alternative. This section reviews representative approaches based on hand-crafted descriptors and deep learning, and introduces inventory-based localization as a compact alternative. We highlight their limitations in forests to motivate our inventory-based formulation.

Hand-crafted Descriptors-based Localization: Conventional place recognition methods based on hand-crafted descriptors are typically divided into global and local approaches. Global descriptors [14–16, 42] compress an individual scan or submap into a compact representation for efficient nearest neighbor search. Early methods such as M2DP [43] rely on multi-view density projections, while later approaches increasingly adopt BEV projections as spatial representations. Scan Context [14] uses a polar grid to encode the maximum elevation in each cell. Scan Context++ [15] augments Scan Context with Cartesian projections for metric localization. Other methods, including RING [44] and RING++ [42], apply the Radon transform to decouple yaw and translation, and SOLiD [16] encodes scans in azimuth–elevation space. While efficient in urban environments, these global descriptors perform poorly in forests due to structural similarity and sensor variability such as angular resolution and mounting height, which lead to inconsistent projections and degraded robustness.

Local descriptors aim to improve geometric distinctiveness by focusing on salient regions. Classical descriptors like FPFH [45] and SHOT [46] capture local features but lack global retrieval capabilities and are typically integrated into voting-based frameworks [47]. In forests, dense and structureless vegetation results in numerous indistinct keypoints, increasing computational cost and false positives. To improve efficiency, projection-based methods have been proposed; for instance, MapClosure [19, 48] extracts ORB [49] features from ground-projected BEV images for (x, y, yaw) estimation, while aligning ground normals for $(\text{roll}, \text{pitch}, z)$. However, the assumption of there being an observable ground plane fails in natural environments. Triangle-based meth-

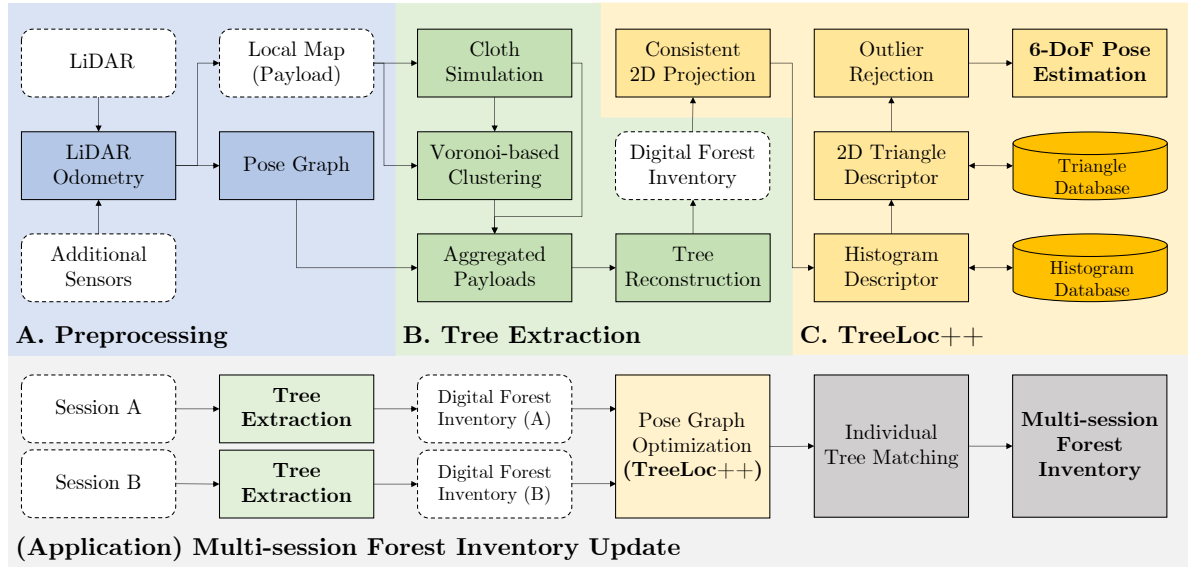


FIGURE 2: Pipeline of TreeLoc++. TreeLoc++ extracts tree-level traits using RealtimeTrees and converts them into two descriptors for place recognition. Based on the retrieved candidates, it estimates the full 6-DoF pose while suppressing outliers arising from incorrect triangle matches. Using the resulting global localization, trees observed across multiple sessions can be associated, enabling consistent matching and incremental updates of tree traits.

ods [17, 18] utilize hash-based indexing, but the performance deteriorates due to unstable feature extraction from foliage and the lack of distinctive geometric structures. Intensity- and reflectivity-aware extensions [50, 51] offer improvements in urban settings, but provide limited benefit in forests, where those channels exhibit low discriminative variation.

Segment-based methods take a different approach by representing scenes at the object level to enhance robustness. NSM and ESM [27, 28] replace dense point clouds with segment representations, showing promising results in forests. However, their discriminative power remains limited due to the prevalence of similar tree geometries and the lack of explicitly modeled inter-segment spatial relationships.

Learning-based Localization: To address the limitations of hand-crafted descriptors, learning-based methods exploit deep networks for improved place recognition. Point-based methods, such as PointNetVLAD [52], TransLoc3D [53], and LoGG3D-Net [54], aggregate point-wise features into global descriptors. Sparse convolutional architectures [55], as used in MinkLoc3Dv2 [56], improve scalability, while transformer-based models like HOTFormerLoc [57] and ForestLPR [58] capture long-range or vertical tree structure through attention mechanisms and layered BEV encoders.

In parallel, projection-based approaches leverage 2D representations such as BEV or range images to utilize 2D encoders. BEVPlace++ [59] uses rotation-equivariant BEV encoders, and BVMatch [60] performs retrieval in the frequency domain with bag-of-words representations. ImLPR [61] combines multiple-channel range images with vision foundation models [62] to enhance generalization. Additionally, semantic graph-based methods [63, 64] incorporate object-level relationships for improved structural reasoning. However, in forest environments, these approaches are

unreliable due to high scene similarity that leads to aliasing, and the noise-prone nature of semantic segmentation.

Beyond retrieval, some methods integrate verification or pose estimation into the localization pipeline. SGV [65] evaluates correspondence consistency without requiring explicit registration, while end-to-end frameworks like LCDNet [66] and EgoNN [67] jointly estimate loop closure probability and relative pose. While effective in structured settings, these methods often struggle in forests due to domain shift and inconsistent local feature extraction in cluttered scenes.

Inventory-based Localization: To overcome the limitations of dense representations, recent work explores DFIs as compact, interpretable priors for localization that encode tree attributes such as position, orientation, and DBH. TreeLoc [29] proposes a DFI-based localization framework using TDH and triangle descriptors for structural encoding, but its performance degrades in repetitive stem layouts due to ambiguous correspondences. Similarly, Tremblay and Béland [68] perform marker-free registration via stem-triplet matching; however, since it relies only on inter-stem distances and DBH consistency, it remains vulnerable to structural ambiguity. Liang et al. [69] also use stem centers and triangle relationships, but are limited to planar alignment and do not exploit additional tree attributes. Their method relies on brute-force triangle matching and repeatedly applies the transformation estimated from each triangle correspondence to all stem centers for verification, resulting in high computational cost. TreeLoc++ tackles these issues by refining correspondences through lightweight DBH filtering and yaw-consistent inlier voting. It also enables stable 6-DoF localization using only DFIs, without raw point clouds or training on large datasets, making it suitable for scalable localization.

III. System of TreeLoc++

Fig. 2 shows the overall pipeline of TreeLoc++. The system begins with tree reconstruction from LiDAR scans and associated poses, generating a DFI. Based on this representation, localization is performed in three stages: (i) preprocessing, which projects tree locations onto a consistent 2D plane estimated from stem axes; (ii) place recognition, which retrieves candidate revisits through a coarse-to-fine matching strategy; and (iii) pose estimation, which performs geometric verification and refinement using robust filtering methods.

A. Digital Forest Inventory Construction

1) Tree Extraction

To ensure sufficient point density for reliable tree segmentation and modeling, TreeLoc++ aggregates k consecutive LiDAR scans into a local submap called a payload, where each payload overlaps with the previous one by v scans to maintain spatial continuity. These payloads are generated only when the system is moving to avoid redundant accumulation. The scan poses are obtained from a local trajectory, which a LiDAR-based SLAM system can provide.

Let \mathcal{P}_u denote the payload indexed by u . For a given index t , we define a window of s payloads as $\mathcal{W}_t = \{t - \lfloor \frac{s-1}{2} \rfloor, \dots, t + \lfloor \frac{s-1}{2} \rfloor\}$. These payloads are transformed into a common local frame and aggregated into a submap $\mathcal{Z}_t = \bigcup_{u \in \mathcal{W}_t} \mathbf{T}_{t \leftarrow u} \cdot \mathcal{P}_u$, where $\mathbf{T}_{t \leftarrow u}$ transforms each payload into the reference frame of \mathcal{P}_t . This submap-based approach, illustrated in Fig. 3, provides the dense geometric input required for subsequent tree modeling.

Tree instances are extracted from \mathcal{Z}_t using RealtimeTrees [35] through terrain normalization and cylindrical fitting. Instead of restating the underlying segmentation mechanics, we refer the reader to [35] for further details on the fitness functions and non-maximum suppression strategies used for stem axis detection. For all verified clusters, stem profiles are estimated by fitting 2D circles to vertical slices via a randomized Hough transform. These instances are then classified based on geometric completeness, where only those satisfying minimum observation range and angular span requirements are considered successfully reconstructed, while the remainder are retained as candidate stems. The resulting collection of trees and their associated geometric attributes constitutes the DFI, which serves as the fundamental data structure for subsequent localization.

2) Digital Forest Inventory for Localization

TreeLoc++ operates in two distinct inventory modes: local and global. As illustrated in the upper part of Fig. 3, the local inventory mode aggregates payloads within a temporal window \mathcal{W}_t to support incremental tasks such as SLAM loop closure or multi-robot localization. Conversely, the global mode merges all mission payloads into a single window $\mathcal{W}_{\text{global}}$, where trees are extracted once over the entire dataset as shown in the lower part of Fig. 3. For

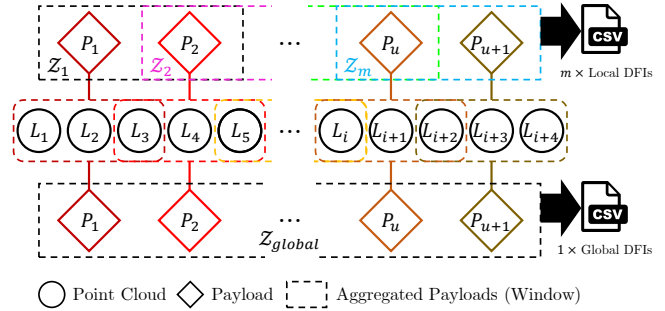


FIGURE 3: Payload-based forest inventory generation. (Top) Payloads are aggregated over temporal windows to form local inventories along the trajectory. (Bottom) All payloads are merged into a global inventory, which is queried at sampled poses to generate local inventories for localization.

localization, the global inventory is queried at selected poses, such as trajectory points or spatially sampled locations, to extract nearby trees within a fixed radius. Whether derived from local windows or queried from the global mode, the resulting forest inventory is always transformed into the local coordinate frame of the corresponding pose to ensure consistent descriptor generation. This design enables the reuse of globally consistent tree data for large-scale, multi-session registration and long-term mapping applications.

For each reconstructed tree, we extract its 3D stem orientation $\mathbf{A}_j \in \text{SO}(3)$ and DBH d_j . The stem position $\mathbf{p}'_j \in \mathbb{R}^3$ is defined by its horizontal stem center \mathbf{c}'_j and base height \mathbf{b}'_j , determined by the terrain elevation at the stem center. An inventory at time t is represented as $\mathcal{M}_t = (\mathbf{T}_t, \mathcal{I}_t)$, where \mathbf{T}_t is the system pose and $\mathcal{I}_t = \{(\mathbf{A}_j, \mathbf{p}'_j, d_j)\}_{j=1}^{n_t}$ is the set of n_t tree attributes. These attributes are computed per aggregated payloads \mathcal{Z}_t from RealtimeTrees.

To ensure a sufficient number of trees for descriptor generation, local inventories are hierarchically augmented only when the tree count falls below a required threshold. The augmentation integrates reconstructed trees from preceding inventories (\mathcal{I}_{t-1} to \mathcal{I}_{t-5}), while filtering duplicates using the local trajectory. It compensates for limited local visibility or segmentation inconsistencies and is omitted in global mode, as the comprehensive aggregation of payloads provides inherently sufficient coverage. If still insufficient, candidate stems are incorporated based on their observation frequency to ensure descriptor stability.

B. Axis-Based Alignment and 2D Projection

To generate compact descriptors from DFI, TreeLoc++ projects stem centers onto a common 2D plane derived from the forest inventory \mathcal{I}_t . This removes height ambiguity while preserving stable inter-tree geometry, which is more reliable for place recognition. However, roll and pitch variations across viewpoints distort the local xy -plane of LiDAR scans, leading to inconsistent projections.

Ground-plane fitting is often used to correct such distortion but is unreliable in forests with uneven or partially observed terrain. As shown in Fig. 4, ground-based alignment may work in some views but fail in others due to inconsistent

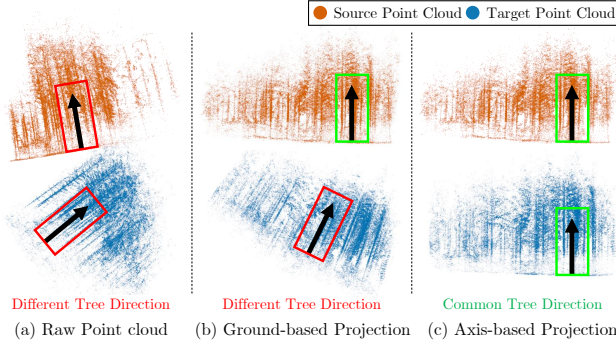


FIGURE 4: Comparison of alignment strategies for 2D projection. Arrows indicate the estimated vertical direction. (a) Raw point clouds show inconsistent orientation. (b) Ground-based alignment is inconsistent across views. (c) Axis-based alignment using tree stems yields consistent orientation.

terrain estimation. In contrast, alignment using stem axes provides a consistent frame across varying viewpoints. We therefore align each frame using the stem axes of reconstructed trees. For each tree j , we extract a unit vector \mathbf{a}_j from the third column of its orientation matrix $\mathbf{A}_j \in \text{SO}(3)$. A rotation $\mathbf{R}_t^A \in \text{SO}(3)$ is then estimated to align the axes $\{\mathbf{a}_j\}$ to a reference direction $\mathbf{v} \in \mathbb{S}^2$ by solving

$$\mathbf{R}_t^A = \arg \min_{\mathbf{R} \in \text{SO}(3)} \sum_j (1 - |\mathbf{v}^\top \mathbf{R} \mathbf{a}_j|)^2. \quad (1)$$

We set $\mathbf{v} = \mathbf{e}_z = (0, 0, 1)^\top$ in practice, though other directions can be used. This alignment corrects roll and pitch while leaving yaw unconstrained, which retains stable horizontal inter-tree geometry. Notably, the alignment remains valid under an unknown global viewpoint rotation \mathbf{R}_{view} , since applying (1) to the rotated axes $\tilde{\mathbf{a}}_j = \mathbf{R}_{\text{view}} \mathbf{a}_j$ yields an alignment that cancels the effect of \mathbf{R}_{view} and restores a consistent projection frame. After estimating \mathbf{R}_t^A , each stem center \mathbf{p}'_j is transformed to the aligned frame as $\mathbf{p}_j = \mathbf{R}_t^A \mathbf{p}'_j$.

To obtain 2D coordinates for descriptor generation, the aligned stem \mathbf{p}_j are projected onto the plane orthogonal to \mathbf{v} using an orthonormal basis $\{\mathbf{u}_1, \mathbf{u}_2\}$ satisfying $\mathbf{u}_i^\top \mathbf{v} = 0$, resulting in projected coordinates $\mathbf{c}_j = [\mathbf{u}_1^\top; \mathbf{u}_2^\top] \mathbf{p}_j \in \mathbb{R}^2$. In the special case where $\mathbf{v} = \mathbf{e}_z$, this simplifies to:

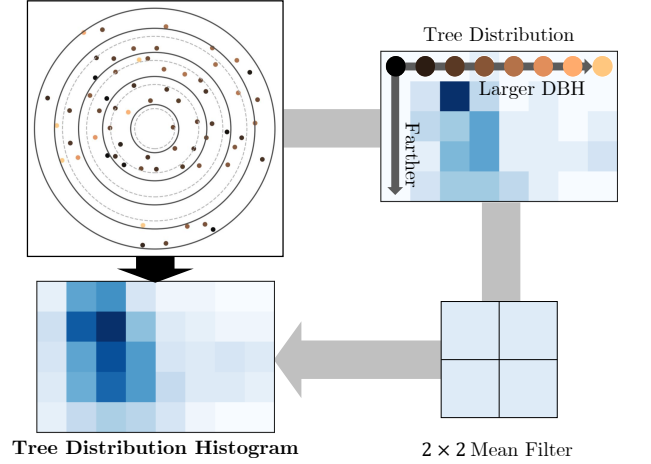
$$\mathbf{c}_j = \begin{bmatrix} 1 & 0 & 0 \\ 0 & 1 & 0 \end{bmatrix} (\mathbf{p}_j - (\mathbf{e}_z^\top \mathbf{p}_j) \mathbf{e}_z), \quad (2)$$

yielding a roll- and pitch-invariant 2D representation.

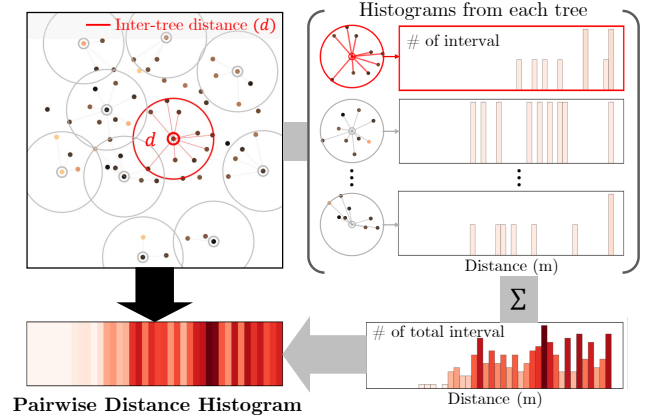
C. Coarse Retrieval via Tree-Based Histograms

To enable efficient and robust place recognition, we summarize the spatial structure of each inventory using two complementary histogram descriptors, TDH and PDH, computed from the reconstructed trees \mathcal{I}_t , as illustrated in Fig. 5.

Firstly, TDH encodes 2D spatial structure by assigning each tree to overlapping radial and DBH bins based on its stem center $\{\mathbf{c}_j\}$ and diameter $\{d_j\}$. Radial bins partition $[r_{\min}, r_{\max}]$ into n_r intervals with overlap w_r , while DBH bins partition $[d_{\min}, d_{\max}]$ into n_d intervals with overlap w_d . The resulting histogram $\mathbf{H}_t \in \mathbb{R}^{n_r \times n_d}$ is smoothed



(a) Tree Distribution Histogram (TDH) Generation



(b) Pairwise Distance Histogram (PDH) Generation

FIGURE 5: Generation of histogram descriptors. (a) TDH encodes tree distributions using overlapping radial and DBH bins. Each radial bin spans from a dashed circle to the second subsequent solid circle, illustrating the overlapping construction. (b) PDH aggregates inter-tree distance histograms computed for each tree into a 1D scene-level representation.

with a 2×2 uniform kernel and flattened into a 40-dimensional descriptor. Overlap parameters and smoothing improve robustness to noise and pose variation.

While TDH captures tree attributes via spatial binning, it lacks inter-tree relationships and is sensitive to the choice of reference center, varying with missing trees or slight shifts in their positions. To address this, we introduce PDH, a 1D histogram that encodes local structure by aggregating pairwise Euclidean distances between stem centers. Distances are binned over $[l_{\min}, l_{\max}]$ into n_{bins} intervals, yielding a 40-dimensional descriptor invariant to rotation and translation. Although structural perturbations may affect some distances, the aggregation distributes their impact across many bins, reducing sensitivity to local changes. Compared to TDH, PDH produces less sparse and more stable histograms, retrieving more true positives and complementing TDH.

For each query inventory at index t , both descriptors are compared against the database. Let $\mathbf{h}_t^{\text{TDH}}$ and $\mathbf{h}_t^{\text{PDH}}$

denote the query descriptors, and $\mathbf{h}_i^{\text{TDH}}$, $\mathbf{h}_i^{\text{PDH}}$ those of a candidate i . Descriptor distances are computed using the chi-square metric χ^2 as $d_i^{\text{TDH}} = \chi^2(\mathbf{h}_i^{\text{TDH}}, \mathbf{h}_i^{\text{TDH}})$ and $d_i^{\text{PDH}} = \chi^2(\mathbf{h}_i^{\text{PDH}}, \mathbf{h}_i^{\text{PDH}})$. Each distance is min-max normalized to balance the influence of TDH and PDH, with the result denoted as \hat{d}_i . The retrieval score is defined as $\text{score}_i = -(\hat{d}_i^{\text{TDH}} + \hat{d}_i^{\text{PDH}})$, such that lower descriptor distances yield higher scores. The top 100 candidates are retained for fine-grained retrieval.

D. 2D Triangle Descriptor Using Tree Centers

To refine candidates from histogram-based coarse retrieval, we introduce a 2D triangle descriptor that is rotation- and translation-invariant, capturing local inter-tree geometry. Following geometric hashing principles [18], the descriptor is constructed from the aligned 2D stem centers.

For each center \mathbf{c}_i , we select its m nearest neighbors and form triangles by combining \mathbf{c}_i with each unordered neighbor pair $(\mathbf{c}_j, \mathbf{c}_k)$. Each triangle is represented by its side lengths $(\ell_{ij}, \ell_{jk}, \ell_{ik})$, sorted in ascending order as (ℓ_1, ℓ_2, ℓ_3) for permutation invariance. The triangle area A is also computed to enhance distinctiveness. All geometric quantities are quantized with resolution δ_ℓ as $\ell_i^q = \lfloor \ell_i / \delta_\ell \rfloor$ and $A^q = \lfloor A / \delta_\ell \rfloor$. The final triangle hash is computed by:

$$\begin{aligned} h'_{ijk} &= ((\ell_3^q \cdot \rho + \ell_2^q) \bmod U \cdot \rho + \ell_1^q) \bmod U, \\ h_{ijk} &= (h'_{ijk} \cdot \rho + A^q) \bmod U. \end{aligned} \quad (3)$$

where ρ is a large prime and U is the maximum hash range. These hashes index triangles for efficient matching.

Metadata $\mathbf{D}_{ijk} = \{\mathcal{A}_i, \mathcal{A}_j, \mathcal{A}_k, \mathbf{q}_{ijk}, s\}$ is stored in each triangle, where \mathcal{A} contains tree attributes, \mathbf{q}_{ijk} is the triangle centroid, and s is the scene index. This metadata supports subsequent geometric verification in later stages.

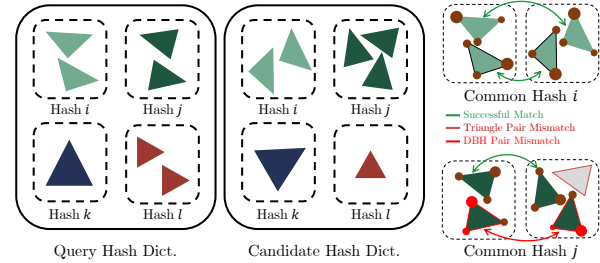
For each scene s , we store the multiset of triangle hashes $\mathcal{H}_s = \{h_{ijk}\}$. Let \mathcal{K}_s denote the set of unique hash keys in \mathcal{H}_s . During fine retrieval, a query scene Q is compared with a candidate scene C by counting shared triangle hashes:

$$S(Q, C) = \sum_{h \in \mathcal{K}_Q \cap \mathcal{K}_C} \min(\text{freq}_Q(h), \text{freq}_C(h)), \quad (4)$$

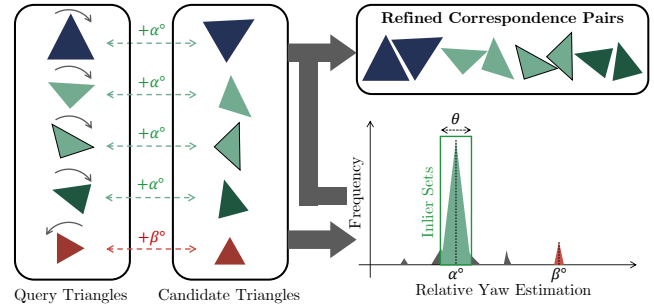
where $\text{freq}_Q(h)$ and $\text{freq}_C(h)$ are the occurrences of hash h in \mathcal{H}_Q and \mathcal{H}_C , respectively. Unlike simple set intersection, multiset-based scoring accounts for repeated geometric patterns, improving similarity discrimination. The top 10 candidates ranked by $S(Q, C)$ proceed to geometric verification.

E. Outlier Rejection via DBH Filtering and Yaw Voting

To extract an inlier set for geometric verification, we refine the triangle matches. Ambiguous hash collisions can produce false correspondences, which often manifest as attribute- or pose-inconsistent matches. We suppress these outliers through DBH filtering and yaw voting.



(a) DBH Filtering for Hash Collision



(b) Yaw Voting for Outlier Suppression

FIGURE 6: Inlier set selection via DBH filtering and yaw voting. (a) Ambiguous triangle correspondences sharing the same hash are disambiguated using DBH consistency. (b) Yaw angles from remaining correspondences are aggregated, and only those consistent with the dominant yaw are retained.

1) Outlier Rejection via DBH Filtering

When a common hash value appears multiple times, it is unclear which triangles should be matched, as shown in Fig. 6a. Let m and n be the numbers of triangles in the query and candidate scenes sharing a given hash. In such cases, at most $\min(m, n)$ valid correspondences can exist.

To resolve this ambiguity, we use the triangle DBH from metadata \mathbf{D} . Let $\mathbf{d}_Q^i = (d_{Q1}^i, d_{Q2}^i, d_{Q3}^i)$ and $\mathbf{d}_C^j = (d_{C1}^j, d_{C2}^j, d_{C3}^j)$ be the DBH vectors of the i -th and j -th triangles. Since DBH vectors follow the sorted side length order, we can directly compare them and define the matching cost as

$$\Delta_{ij} = \sum_{v=1}^3 \left| d_{Qv}^i - d_{Cv}^j \right|. \quad (5)$$

We select up to $\min(m, n)$ one-to-one correspondences with minimum total cost and reject pairs violating τ_{DBH} :

$$\max_{v \in \{1,2,3\}} \left| d_{Qv}^i - d_{Cv}^j \right| < \tau_{\text{DBH}}. \quad (6)$$

2) Yaw-Consistent Inlier Voting

Even after DBH filtering, repetitive local structures may still include incorrect correspondences that induce erroneous pose estimates. To enforce global consistency, we analyze the relative yaw rotation implied by each remaining triangle match as shown in Fig. 6b.

For each matched triangle pair, a 2D rigid transformation is estimated using singular value decomposition (SVD)-

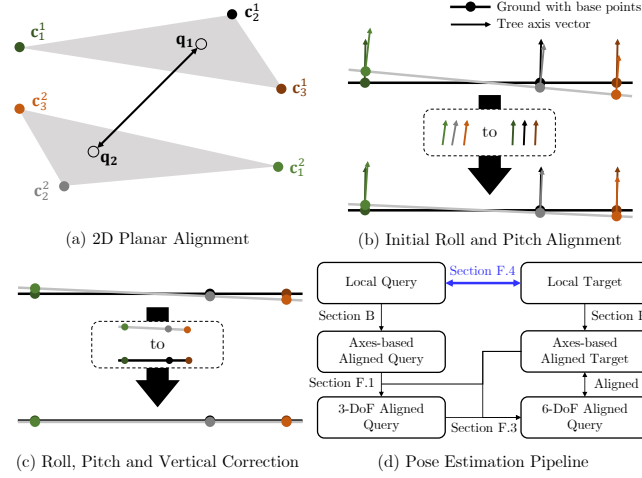


FIGURE 7: Pose estimation pipeline. (a) Initial 2D planar alignment is estimated using triangle correspondences. (b) Roll and pitch are aligned using the axes of matched trees. (c) Vertical correction is performed by jointly refining height together with roll and pitch. (d) The final 6-DoF transformation is obtained, summarizing the overall pose estimation process.

based alignment, from which the relative yaw θ_k is extracted. We exclude matches that yield a reflection with $\det(\mathbf{R}_k) < 0$. The remaining angles are accumulated into a histogram to identify the dominant yaw θ^* . The final inlier set is defined as:

$$\mathcal{I} = \{k \mid |\theta_k - \theta^*| < \tau_{\text{yaw}}\}, \quad (7)$$

where τ_{yaw} is a predefined angular threshold.

This two-step process, DBH-based disambiguation followed by yaw voting, produces a correspondence set consistent in both local attributes and global pose. The resulting inlier set is then used for geometric verification and 6-DoF pose estimation.

F. Geometric Verification and 6-DoF Pose Estimation

We estimate the 6-DoF relative transformation between a query scene \mathcal{I}_Q and a candidate scene \mathcal{I}_C . Planar alignment, vertical correction, and 6-DoF transformation estimation are performed sequentially. This process is applied to the top 10 candidates retrieved via triangle hash matching, and the best match is selected through geometric verification. An overview of the pipeline is shown in Fig. 7.

1) Planar Alignment via Inlier Triangles and IRLS Refinement
Using the inlier triangle correspondences, we extract the matched centroids $\{(\mathbf{q}_u^Q, \mathbf{q}_u^C)\}_{u=1}^N$ from metadata \mathbf{D} and estimate an initial planar transformation $\mathbf{T}_{C \leftarrow Q}^{\text{init}} \in \text{SE}(2)$, parameterized by $(\mathbf{R}_{2D}^{\text{init}}, \mathbf{t}_{2D}^{\text{init}})$, via least-squares alignment:

$$\mathbf{R}_{2D}^{\text{init}}, \mathbf{t}_{2D}^{\text{init}} = \arg \min_{\mathbf{R}, \mathbf{t}} \sum_{u=1}^N \|\mathbf{q}_u^C - (\mathbf{R}\mathbf{q}_u^Q + \mathbf{t})\|^2. \quad (8)$$

This initial estimate $\mathbf{T}_{C \leftarrow Q}^{\text{init}}$ is further optimized using iteratively reweighted least squares (IRLS) to improve robustness

by down-weighting outlier residuals. IRLS is initialized with $(\mathbf{R}_{2D}^{\text{init}}, \mathbf{t}_{2D}^{\text{init}})$, and we refine the planar transformation over all vertex-level matches $(\mathbf{c}_i^Q, \mathbf{c}_i^C)$ in corresponding triangles:

$$\mathbf{R}_{2D}, \mathbf{t}_{2D} = \arg \min_{\mathbf{R}, \mathbf{t}} \sum_i w_i \|\mathbf{c}_i^C - (\mathbf{R}\mathbf{c}_i^Q + \mathbf{t})\|^2. \quad (9)$$

where weights w_i follow a Huber kernel based on residuals.

2) Tree-Level Correspondences and Roll-Pitch Estimation

Applying the planar alignment, each query \mathbf{c}_i^Q is transformed as $\tilde{\mathbf{c}}_i = \mathbf{R}_{2D}\mathbf{c}_i^Q + \mathbf{t}_{2D}$. Tree-level correspondences are then established by finding candidate matches \mathbf{c}_j^C via nearest-neighbor search, subject to spatial and DBH thresholds:

$$\|\tilde{\mathbf{c}}_i - \mathbf{c}_j^C\| < \tau_d, \quad |d_i^Q - d_j^C| < \tau_{\text{DBH}}. \quad (10)$$

Using the matched pairs $\mathcal{M} = \{(i, j)\}$, we solve (9) once to update $(\mathbf{R}_{2D}, \mathbf{t}_{2D})$. The same set \mathcal{M} is used to estimate roll and pitch by aligning axis vectors \mathbf{a}_i^Q and \mathbf{a}_j^C . With yaw fixed by \mathbf{R}_z extracted from \mathbf{R}_{2D} , we estimate the residual roll-pitch rotation $\mathbf{R}_{\phi, \psi}$ via RANSAC over tree axis correspondences:

$$\mathbf{R}_{\phi, \psi} = \arg \min_{\mathbf{R}} \sum_{(i, j) \in \mathcal{M}} \left(1 - (\mathbf{a}_j^C)^\top \mathbf{R} \mathbf{R}_z \mathbf{a}_i^Q\right). \quad (11)$$

3) Vertical Correction and Final Scoring

Thanks to the roll-pitch estimation using tree axis, the remaining roll-pitch error is small. This justifies the use of a small-angle approximation when modeling vertical misalignment. For a 3D point (x, y, z) , the effect of roll (ϕ) and pitch (ψ) on the vertical coordinate is given by

$$z' = -x \cos \phi \sin \psi + y \sin \phi + z \cos \phi \cos \psi. \quad (12)$$

Yaw is omitted as it does not affect the vertical component. For small ϕ and ψ , this approximates to $z' \approx z - \psi x + \phi y$.

Using tree base heights, the vertical relationship between a matched tree pair $(i, j) \in \mathcal{M}$ is approximated as

$$b_j^C \approx \tilde{b}_i^Q, \quad \tilde{b}_i^Q = \hat{b}_i^Q + \Delta z - \Delta \psi \hat{x}_i^Q + \Delta \phi \hat{y}_i^Q, \quad (13)$$

where $(\Delta z, \Delta \phi, \Delta \psi)$ denote the global vertical offset and small residual roll-pitch corrections, and (\hat{x}_i, \hat{y}_i) and \hat{b}_i^Q denote the planar coordinates and base height of the query tree after applying the planar alignment \mathbf{T}_{2D} and the roll-pitch correction $\mathbf{R}_{\phi, \psi}$. The parameters $(\Delta z, \Delta \phi, \Delta \psi)$ are estimated by minimizing the residual $r_{ij} = b_j^C - \tilde{b}_i^Q$ over all matched pairs $(i, j) \in \mathcal{M}$ using a RANSAC-based least-squares estimator for robustness. The resulting correction is expressed as a 3D transformation:

$$\mathbf{T}_{6D} = \begin{bmatrix} \mathbf{R}_{\Delta \phi, \Delta \psi} \mathbf{R}_{\phi, \psi} & [0, 0, \Delta z]^\top \\ \mathbf{0} & 1 \end{bmatrix} \mathbf{T}_{3D}, \quad (14)$$

where \mathbf{T}_{3D} denotes the 2D alignment \mathbf{T}_{2D} lifted to $\text{SE}(3)$.

TABLE 1: Summary of datasets used for evaluation.

Dataset / Sequence	Length	Environment Characteristics
Oxford Forest Place Recognition	Evo:Single	1.53 km Tall mixed-species forest, moderate density
	Stein am Rhein	0.70 km Sparse coniferous trees, flat terrain
	Wytham	0.70 km Ground vegetation with cluttered trees, severe occlusion
	Forest of Dean	0.75 km Widely spaced oak trees, minimal ground vegetation
	Evo23:00-05	4.69 km Same forest as Evo, different traversals
Ours	Evo25:00-08	3.29 km Same forest as Evo, vegetation growth, seasonal change
Wild-Places	Venman01-04	12.68 km Moderate vegetation density, mixed terrain, relatively stable appearance
	Karawatha01-04	20.24 km Dense vegetation, uneven terrain, pronounced appearance changes

4) Final 6-DoF Transformation in Local Frames

All transformations so far are computed in the reference-aligned frame, where roll and pitch are aligned using tree axis-based 2D projection. To recover the full 6-DoF transformation between the original local frames, we undo this alignment using the corresponding rotations \mathbf{R}_Q^A and \mathbf{R}_C^A .

Let $\mathbf{T}_Q^A = \text{diag}(\mathbf{R}_Q^A, 1)$ and $\mathbf{T}_C^A = \text{diag}(\mathbf{R}_C^A, 1)$. The final transformation from the query to the candidate frame is given by $\mathbf{T}_{C \leftarrow Q}^{6D} = (\mathbf{T}_C^A)^{-1} \mathbf{T}_{6D} \mathbf{T}_Q^A$. This yields a global 6-DoF relative pose purely from tree-level geometric information.

To assess alignment quality and select the best match, we compute an overlap score combining geometric consistency and spatial proximity:

$$\mathcal{O}(Q, C) = \frac{|\mathcal{M}_{Q,C}|}{|\mathcal{T}_Q| + |\mathcal{T}_C| - |\mathcal{M}_{Q,C}|} \cdot p(\|\mathbf{t}\|), \quad (15)$$

where $|\mathcal{M}_{Q,C}|$ is the number of matched trees, and $|\mathcal{T}_Q|$, $|\mathcal{T}_C|$ are the tree counts in the query and candidate scenes.

The penalty term $p(\|\mathbf{t}\|) = \exp(-\|\mathbf{t}\|^2/\sigma_t^2)$ imposes a spatial prior that favors candidates with smaller estimated planar displacement \mathbf{t} from $\mathbf{T}_{C \leftarrow Q}^{6D}$, where σ_t is a scaling parameter controlling the spatial constraint. This reflects the intuition that large translation shifts often lead to discrepancies in reconstruction quality; as the same tree is viewed from significantly different distances or angles, varying degrees of occlusion and sparsity degrade its geometric consistency. The candidate with the highest score $\mathcal{O}(Q, C)$ is selected, along with its estimated transformation $\mathbf{T}_{C \leftarrow Q}^{6D}$.

IV. Datasets and Evaluation Metrics

A. Dataset Summary

We evaluated TreeLoc++ on 27 sequences collected across diverse forest environments, including both complete plot



FIGURE 8: Example scenes for each dataset and sequence.

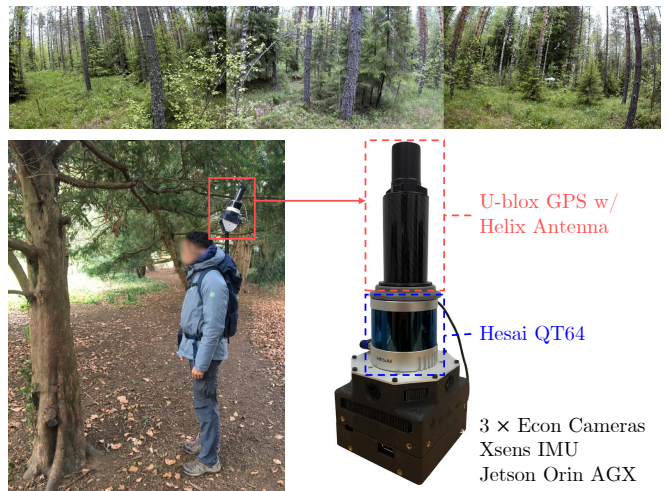


FIGURE 9: Overview of the Evo25 and acquisition platform. (Top) Example scenes captured in Evo25. (Bottom) Backpack-based data acquisition system equipped with a LiDAR, IMU, GPS antenna, and three cameras.

mappings and point-to-point route traversals. Dataset characteristics are summarized in Table. 1 and Fig. 8.

We first utilized the Oxford Forest Place Recognition dataset [23], which contains ten sequences collected from small forest plots across three countries. All data were recorded using a backpack-mounted platform that incurs significant roll and pitch motion while being carried during recording, presenting a further challenge for localization.

To assess long-term performance under significant appearance changes, we also introduce nine newer sequences, Evo25:00-08, collected two years later in the same forest as Evo:Single. This dataset captured environmental changes caused by vegetation growth and seasonal variation, facilitating the evaluation of long-term global localization. Ground truth trajectories for Evo25 were obtained via multi-session alignment, with details provided in the Appendix A. An overview of the data acquisition setup is shown in Fig. 9.

To complement the plot inventory datasets, we used the Wild-Places dataset [39], which consists of eight sequences recorded in two large-scale forest parks in Australia: Venman01-04 and Karawatha01-04. These sequences

TABLE 2: (Exp A-1) Intra-session place recognition performance in Oxford Forest Place Recognition Dataset. **Bold**: Best, *Italic*: Second-best.

Dimension / Method		Evo:Single				Forest of Dean			
		R@1	MR	MF1	AUC	R@1	MR	MF1	AUC
Learning-based (Wild-Places)	TransLoc3D	0.425	0.001	0.596	0.570	0.570	0.002	0.726	0.659
	LoGG3D-Net	0.521	0.082	0.685	0.722	<i>0.776</i>	0.182	0.874	0.776
	MinkLoc3Dv2	0.470	0.010	0.608	0.462	0.492	0.058	0.652	0.582
	BEVPlace++	0.872	0.351	0.932	0.973	0.712	0.212	0.837	0.858
	ForestLPR	0.465	0.001	0.635	0.611	0.439	0.058	0.610	0.567
	HOTFormerLoc	0.530	0.019	0.743	0.820	0.583	0.126	0.748	0.780
Hand-crafted (Untrained)	SC++	0.347	0.326	0.762	0.696	0.426	0.333	0.759	0.862
	SOLID	0.222	0.000	0.372	0.352	0.155	0.071	0.367	0.388
	RING++	0.567	0.126	0.223	0.125	0.674	0.194	0.781	0.718
	BTC	0.553	<i>0.531</i>	0.761	0.864	0.559	<i>0.772</i>	0.720	0.692
	MapClosure	0.359	0.064	0.528	0.359	0.166	0.014	0.285	0.154
	TreeLoc	<i>0.890</i>	0.228	<i>0.955</i>	<i>0.984</i>	0.348	0.045	<i>0.897</i>	<i>0.891</i>
	TreeLoc++	0.956	0.933	0.991	0.999	0.891	0.898	0.985	0.997

span substantially longer, forest access road trajectories with temporal gaps, enabling large-scale evaluation.

B. Baselines and Evaluation Protocol

To ensure fair evaluation, we standardized input preprocessing across all methods, including trajectory estimation and submap construction. We first estimated the poses used for payload aggregation and forest inventory generation. To reflect a realistic setup where localization operates alongside online state estimation, we used FAST-LIO2 [70] for Evo:Single and Stein am Rhein, and DLIO [71] for the remaining Oxford sequences. For Wild-Places, ground truth poses were used. Then, scans were aggregated into payloads and accumulated over time to form pose-centric submaps, from which forest inventories were generated. All methods used consistent spatial cropping centered at the query pose, with regions of $30\text{ m} \times 30\text{ m}$ for Oxford and $60\text{ m} \times 60\text{ m}$ for Wild-Places to account for its larger scale.

In our intra-session evaluation, both queries and candidates used local inventory mode. For inter-session evaluation, we considered three configurations: local-local, local-global (with uniformly sampled global poses), and global-global (with inventories from a reference trajectory). For global baselines, the full point clouds were merged to form the global map and then the same cropping was applied during the matching. We compared TreeLoc++ to baselines for place recognition, metric localization, and pose estimation.

Place Recognition: We compared TreeLoc++ with learning-based and hand-crafted methods. Learning-based methods included point-based approaches (TransLoc3D [53], MinkLoc3Dv2 [56], LoGG3D-Net [54], HOTFormerLoc [57]) and the BEV-based methods such as BEVPlace++ [59] and ForestLPR [58]. TransLoc3D and BEVPlace++ were trained on Wild-Places, while the others used pretrained checkpoints. Hand-crafted baselines included global descriptor methods (Scan Context+ [15], SOLiD [16], RING++ [42]), local descriptor methods (BTC [18], MapClosure [48]), and inventory-based method such as TreeLoc [29]. A retrieval was considered correct if within 5 m of the ground truth; additional analyses under varying distance thresholds are

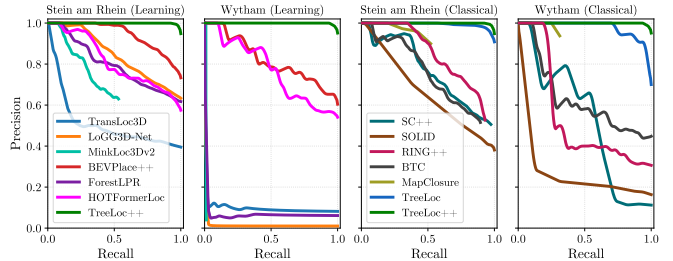


FIGURE 10: (Exp A-1) Precision-Recall curves comparing TreeLoc++ with learning-based (left) and hand-crafted (right) methods. Some learning-based methods outperform hand-crafted baselines but remain below TreeLoc++, while hand-crafted methods show a sharp precision drop at low recall. TreeLoc++ achieves a higher AUC than TreeLoc.

provided in Appendix E. We report Recall@1 (R@1), Maximum Recall at 100% Precision (MR), Maximum F1 score (MF1), and Area Under the Precision-Recall Curve (AUC).

Metric Localization: We evaluated whether each method could recover an accurate pose estimation. LoGG3D-Net and MinkLoc3Dv2 were extended with their feature-based localization, while BEVPlace++ includes its own localization module. Hand-crafted baselines included TreeLoc, RING++, MapClosure, and BTC. As BEVPlace++ and RING++ only estimate (x, y, yaw) , we report both 2D and 3D results. We report Recall@50cm (R@50): the fraction of queries whose estimated pose is within 50 cm and 5° of ground truth, regardless of retrieval correctness. The Success Rate (SR) adds the requirement that the underlying retrieval must also be a true positive. For these successful cases, we report the Average Translation Error (ATE) and Average Rotation Error (ARE). Further benchmark results about pose estimation with registration methods are provided in the Appendix C.

V. Results

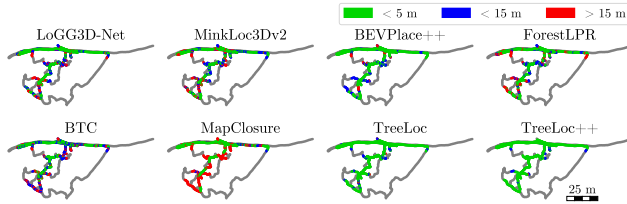
A. Intra-session Place Recognition

1) Oxford Forest: Small and Dense Off-road Forests

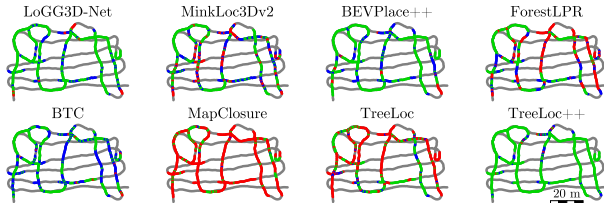
We begin our evaluation with intra-session cases. The first experiment focuses on intra-session place recognition using the Oxford Forest dataset, which consists of short, small-scale off-road sequences characterized by frequent revisits and substantial variations in viewpoint and occlusion.

Evaluation protocol: We compared TreeLoc++ against hand-crafted and learning-based baselines on four sequences. To avoid trivial matches, we excluded the 50 most recent frames from the candidate database.

TreeLoc++: TreeLoc++ achieved the best performance across all metrics (Table. 2), maintaining high precision and the highest MR (Fig. 10). This superior MR is primarily driven by the translation penalty in the overlap score defined in (15). Under frequent revisits and occlusions, where candidates exhibit similar geometry, this penalty favors spatially closer matches and improves true positive retrieval. On Forest of Dean, TreeLoc++ preserved high R@1 despite repetitive geometry; its multiset-based scoring introduced in (4) preserves each tentative triangle match, consistently outperforming TreeLoc as shown in Fig. 11.



(a) Intra-session Matching in Stein am Rhein



(b) Intra-session Matching in Forest of Dean

FIGURE 11: (Exp A-1) Matching results in two sequences. TreeLoc++ identifies the most true positives (green). In failure cases, it still retrieves spatially adjacent candidates (blue) rather than distant false positives (red).

Hand-crafted baselines: Hand-crafted descriptors gave poor performance in these forest sequences. Global descriptor-based methods performed poorly, as compressing entire scans into compact global features limits discriminative power in vertically repetitive and structurally ambiguous scenes. Likewise, local descriptor-based methods suffered from viewpoint sensitivity and unstable keypoint selection. As seen in the PR curves in Fig. 10, these methods exhibited abrupt precision drops or early termination, indicating sensitivity to outliers and reduced matchability.

Learning-based baselines: Learning-based methods show improved performance over hand-crafted baselines as shown in Table. 2 but still suffer from low MR and limited accuracy. While BEVPlace++ is the most competitive, its performance drops sharply in cluttered scenes like Wytham (Fig. 10). As shown in Fig. 11, these methods yield fewer true positives and more near-matches (blue points) than TreeLoc++, failing to distinguish locations accurately. This is primarily due to a persistent domain shift of the training dataset, where inherent structural variations between forests prevent the extraction of robust, generalizable features. A detailed analysis of the impact of training data is provided in the Appendix B.

While the evaluation targets a small-scale setting with frequent revisits, we next consider a more challenging scenario with larger spatial extent and stronger structural aliasing.

2) Wild-Places: Large-scale Forests with Larger Databases

To further validate intra-session place recognition in a more challenging forest environment, we extend our experiments to the Wild-Places dataset. Compared to Oxford, Wild-Places features longer trajectories, larger databases, and fewer revisits, increasing the overall complexity of the task. Moreover, the data are collected along forest access roads, making the dataset less suitable for tree reconstruction. The two sites

TABLE 3: (Exp A-2) Intra-session place recognition performance in Wild-Places.

Category / Method		Venman03			Venman04			Karawatha03		
		R@1	MR	MF1	R@1	MR	MF1	R@1	MR	MF1
Learning-based (Wild-Places)	TransLoc3D	0.632	0.003	0.775	0.801	0.003	0.890	0.693	0.001	0.819
	LoGG3D-Net	0.635	0.000	0.777	0.814	0.113	0.898	0.867	0.009	0.929
	MinkLoc3Dv2	<i>0.722</i>	<i>0.049</i>	<i>0.793</i>	0.853	0.037	0.921	0.814	0.114	0.894
	BEVPlace++	0.354	0.000	0.530	0.885	<i>0.234</i>	0.940	0.842	<i>0.152</i>	0.915
	ForestLPR	0.501	0.025	0.668	0.743	0.045	0.853	0.599	0.010	0.749
	HOTFormerLoc	0.621	0.018	0.766	<i>0.911</i>	0.037	<i>0.953</i>	0.849	0.069	0.921
Hand-crafted (Untrained)	SC++	0.014	0.000	0.222	0.262	0.050	0.494	0.368	0.059	0.583
	SOLID	0.030	0.000	0.060	0.204	0.013	0.453	0.139	0.008	0.267
	RING++	0.123	0.000	0.429	0.301	0.026	0.482	0.411	0.042	0.583
	BTC	0.158	0.030	0.364	0.168	0.061	0.579	0.236	0.022	0.563
	MapClosure	0.180	0.000	0.305	0.741	0.164	0.851	0.585	0.051	0.738
	TreeLoc	0.624	<i>0.057</i>	0.792	0.662	0.016	0.809	0.479	0.017	0.738
	TreeLoc++	0.940	0.978	0.990	0.924	0.980	0.993	0.864	0.897	0.982

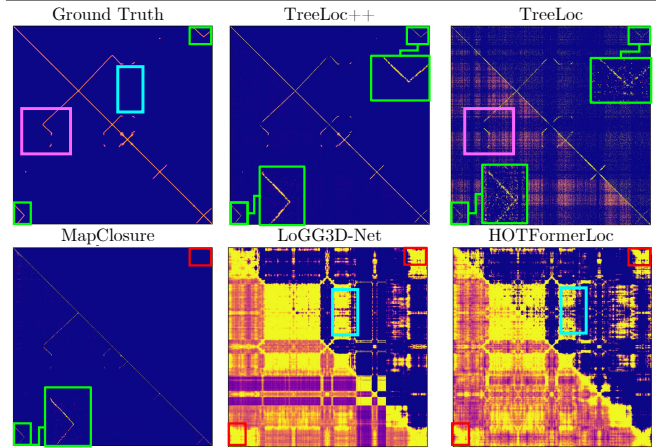


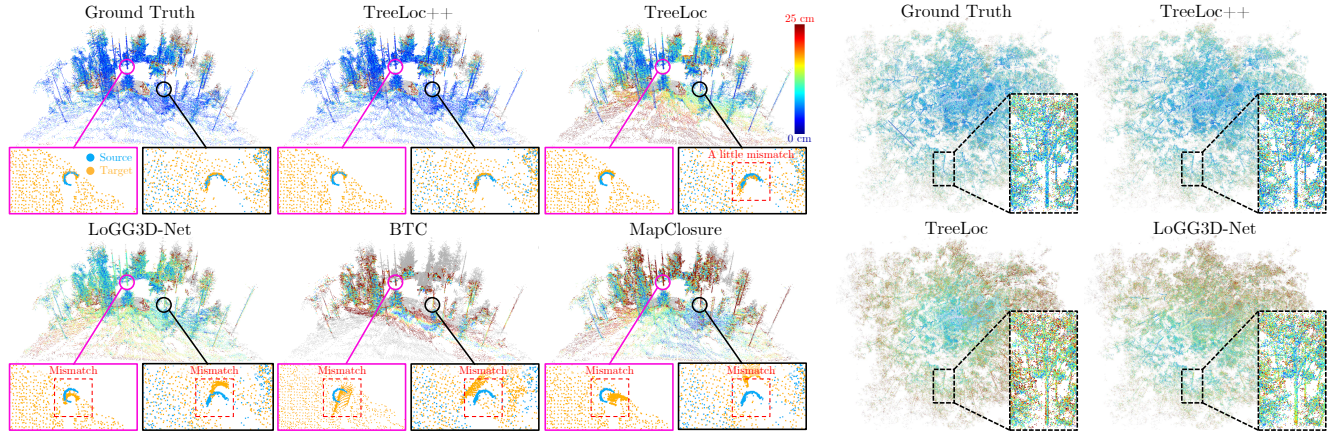
FIGURE 12: (Exp A-2) Feature similarity matrices for Karawatha04 (warmer colors indicate higher similarity). The lower-left and upper-right triangles show mid (20–80%) and high (60–80%) similarities, respectively. TreeLoc++ aligns well with ground truth; others show noisy (pink), low-contrast (red), or spuriously high similarities across unrelated regions (cyan).

present complementary characteristics: Venman exhibits dense, structurally repetitive scenes, whereas Karawatha contains open areas with sparse geometric features.

Evaluation protocol: We utilized four sequences from Wild-Places: Venman03–04 and Karawatha03–04. These sequences were not used to train any of the learning-based baselines. We followed the same intra-session evaluation protocol as used for the Oxford dataset.

Results: As summarized in Table. 3, TreeLoc++ achieved the strongest overall performance on Wild-Places. Despite being less suitable for tree reconstruction, TreeLoc++ forms multiple triangles from common trees for reliable retrieval (Fig. 14), while outlier rejection modules further reduce structural ambiguities that often cause failures in TreeLoc. By contrast, most hand-crafted baselines degrade more on Wild-Places, as they struggle to distinguish structurally similar locations in large databases. Learning-based methods such as LoGG3D-Net and BEVPlace++ achieved relatively high recall on Karawatha03, but lagged behind TreeLoc++ on other metrics due to weaker discrimination.

Similarity analysis: The similarity matrices in Fig. 12 explain both the advantage of TreeLoc++ and the increased



(a) Registration Error in *Evo:Single*

(b) Registration Error in *Karawatha04*

FIGURE 13: **(Exp B)** Registration performance on *Evo* and *Karawatha04*. (a) Point-to-map nearest-neighbor distance after alignment, where *TreeLoc* and *TreeLoc++* achieve low errors and *TreeLoc++* is closest to ground truth. (zoom highlights trunk alignment). (b) In *Karawatha04*, *TreeLoc++* shows blue-dominant patterns consistent with ground truth, while the other methods exhibit red-dominant regions indicating larger residual errors.

TABLE 4: **(Exp B)** Metric-level localization performance on two datasets.

Dimension / Method	Stein am Rhein				Karawatha04				
	R@50	SR	ATE	ARE	R@50	SR	ATE	ARE	
2D	LoGG3D-Net	0.676	0.613	0.150	0.478	0.900	0.860	0.131	0.229
	MinkLoc3Dv2	0.037	0.037	0.310	1.878	0.088	0.088	0.283	1.686
	BEVPlace++	0.853	0.746	0.152	0.644	0.502	0.495	0.217	0.299
	RING++	0.432	0.410	0.206	1.247	0.453	0.401	0.266	0.976
	BTC	0.593	0.386	0.231	0.843	0.527	0.292	0.158	0.422
	MapClosure	0.526	0.479	0.142	0.635	0.638	0.601	0.147	0.489
	<i>TreeLoc</i>	0.976	0.906	0.047	0.197	0.654	0.465	0.055	0.187
	<i>TreeLoc++</i>	0.982	0.941	0.046	0.142	0.924	0.902	0.038	0.140
3D	LoGG3D-Net	0.656	0.599	0.173	1.051	0.891	0.860	0.157	0.510
	MinkLoc3Dv2	0.018	0.018	0.269	2.682	0.046	0.046	0.327	2.540
	BTC	0.310	0.243	0.239	2.219	0.403	0.272	0.227	1.678
	MapClosure	0.526	0.479	0.147	0.756	0.635	0.597	0.148	0.563
	<i>TreeLoc</i>	0.937	0.878	0.121	1.378	0.593	0.423	0.135	1.151
	<i>TreeLoc++</i>	0.939	0.906	0.087	0.470	0.924	0.902	0.068	0.307

difficulty of *Wild-Places* with larger databases. We visualize similarity matrices with 20-80% and 60-80% percentile ranges to highlight overall structure and high-confidence matches, respectively. With larger databases and fewer revisits, true positives become sparse and the separation between true positives and true negatives becomes harder to maintain, making retrieval more challenging. *TreeLoc++* preserves this separation by closely following the ground truth spatial structure, enabling reliable retrieval. In contrast, *TreeLoc* shows lower contrast and more noise, increasing false positives, while *MapClosure* has limited dynamic range, reducing true positives and increasing false negatives. Other global descriptor baselines often assign high similarity to unrelated locations, degrading precision and increasing false positives.

In summary, *TreeLoc++* achieves the strongest intra-session place recognition across diverse forests without training and remains robust across scales.

B. Intra-session Metric Localization

After completing the evaluation of intra-session place recognition on two forest datasets, we turn our attention to another key strength of this work: metric-level localization



FIGURE 14: **(Exp B)** Each row visualizes tree correspondences after geometric verification. *TreeLoc++* establishes matches not only in high-overlap cases (top), but also in moderate (middle) and low-overlap (bottom) scenarios, even beyond the positive threshold, despite complex tree arrangements. This accurate correspondence leads to centimeter-level errors.

performance. In this section, we assess whether each method can recover the relative poses following place recognition.

Evaluation protocol: We evaluated metric localization on four sequences with high R@1 to ensure sufficient true-positive retrievals for downstream pose estimation. Similar to SGV [65], we evaluate *LoGG3D-Net* and *MinkLoc3Dv2* using feature-based correspondence and RANSAC registration. To focus on metric localization, we disable the re-ranking step and estimate the 6-DoF pose directly.

TABLE 5: (Exp C) Inter-session place recognition performance in Wild-Places.

Category / Method		Venman01-04 (12 query-database pairs)								Karawatha01-04 (12 query-database pairs)							
		R@1		MR		MF1		AUC		R@1		MR		MF1		AUC	
		Mean	S	Mean	S	Mean	S	Mean	S	Mean	S	Mean	S	Mean	S	Mean	S
Learning-based (Wild-Places)	TransLoc3D	0.553	0.464	0.008	-0.048	0.707	0.678	0.604	0.511	0.711	1.316	0.013	-0.103	0.831	1.561	0.756	1.268
	LoGG3D-Net	0.660	1.242	0.003	-0.282	0.813	<i>1.382</i>	0.732	0.872	0.897	1.848	0.002	-0.278	<i>0.948</i>	2.299	0.921	<i>1.638</i>
	MinkLoc3Dv2	0.755	0.782	0.033	0.161	0.857	1.030	0.818	0.881	0.849	<i>1.607</i>	0.062	0.150	0.919	1.889	0.911	1.592
	BEVPlace++	0.735	0.701	0.091	-0.025	0.840	0.920	0.841	0.842	0.767	0.934	0.016	-0.193	0.868	1.179	0.767	0.822
	ForestLPR	0.718	0.695	0.023	0.006	0.842	1.006	0.839	1.010	0.790	1.136	0.072	0.024	0.885	1.366	0.885	1.205
	HOTFormerLoc	0.899	1.173	<i>0.155</i>	-0.057	<i>0.946</i>	1.448	<i>0.938</i>	<i>1.350</i>	<i>0.885</i>	1.341	0.088	0.026	0.941	1.628	<i>0.937</i>	1.471
Hand-crafted (Untrained)	SC++	0.245	0.429	0.056	0.129	0.425	0.631	0.396	0.430	0.370	0.632	<i>0.117</i>	0.146	0.560	0.817	0.564	0.704
	SOLID	0.150	0.199	0.014	-0.263	0.288	0.321	0.241	0.093	0.158	0.357	0.000	0.000	0.300	0.501	0.211	0.318
	RING++	0.322	0.448	0.057	-0.004	0.503	0.624	0.500	0.458	0.341	0.713	0.030	-0.143	0.509	0.848	0.402	0.439
	BTC	0.185	0.543	0.006	-0.337	0.331	0.594	0.216	0.338	0.068	0.169	0.005	-0.193	0.221	0.150	0.128	0.024
	MapClosure	0.478	0.338	0.054	-0.008	0.618	0.459	0.465	0.279	0.484	0.420	0.036	-0.121	0.641	0.571	0.479	0.347
	TreeLoc	0.766	0.940	0.046	-0.019	0.890	1.202	0.853	0.954	0.486	0.938	0.003	<i>0.785</i>	0.858	1.747	0.838	1.577
	TreeLoc++	<i>0.896</i>	<i>1.207</i>	0.970	1.469	0.993	2.303	0.998	3.281	0.728	1.266	0.849	1.008	0.974	<i>2.149</i>	0.995	2.801

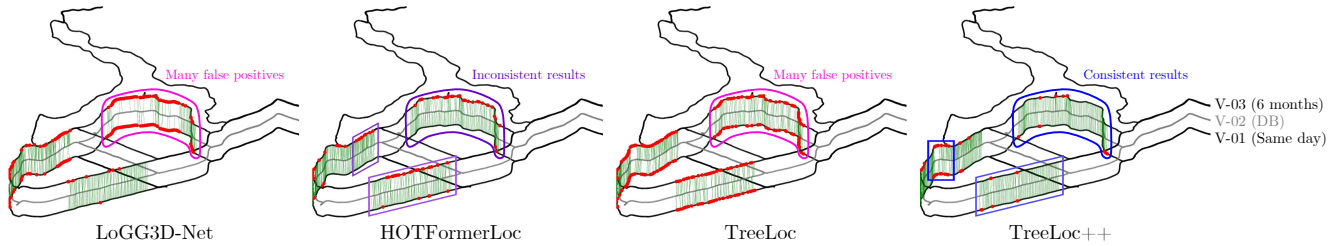


FIGURE 15: (Exp C) Inter-session place recognition on Venman01-03. Following the Wild-Places protocol, evaluation is conducted on unseen regions excluding the training area. LoGG3D-Net and TreeLoc produce numerous false positives (red dots) across sessions (pink). HOTFormerLoc performs well for same-day sequences (Venman01-02) but degrades on Venman03 with a 6-month gap (purple). TreeLoc++ remains consistent across temporal shifts (blue) and retrieves more true positives, even though its false positive regions also appear consistently across sessions.

TreeLoc++: As shown in Table. 4, TreeLoc++ achieved the best overall performance across both 2D and 3D metrics. While TreeLoc performed well in Stein am Rhein, its accuracy dropped in cluttered scenes such as Karawatha04. This degradation was more pronounced in 3D due to TreeLoc’s independent estimation of roll, pitch, and height, which is prone to compounded errors. In contrast, TreeLoc++ jointly estimates these components, yielding more stable and accurate results. Moreover, its high R@50 score indicates successful localization even when the top-1 retrieval does not fall within the evaluation threshold. **BEV and local-descriptor baselines:** BEV-based methods suffered from viewpoint sensitivity and resolution constraints. BEVPlace++ and RING++ do not estimate roll and pitch, causing BEV projections to degrade under viewpoint changes. MapClosure attempts ground-plane compensation but fails under uneven terrain or occlusions (Fig. 4), and ORB-based descriptors on BEV images remain insufficiently distinctive. Similarly, local-descriptor methods such as BTC exhibited unstable feature extraction under vertical variability and occlusions in forest environments.

Learning-based baselines: The localization performance of learning-based methods depended on feature resolution. MinkLoc3Dv2 uses heavily downsampled representations, limiting discriminative power. In the case of LoGG3D-Net,

it retained more spatial detail but still lagged behind TreeLoc++. Learning-based methods also incurred substantial computational overhead, as they must compute pairwise distances between high-dimensional local features to establish feature-level correspondences for metric localization.

Alignment accuracy: To assess alignment accuracy, we evaluated registration on the same set of successful query-match pairs across methods, measuring accuracy via nearest neighbor correspondences within 50 cm. As shown in Fig. 13a, TreeLoc++ produced the most accurate registration, closely similar to the ground truth. TreeLoc and LoGG3D-Net exhibited moderate misalignments, which became more pronounced in cluttered scenes such as Karawatha04 (Fig. 13b). BTC and MapClosure showed severe failures. TreeLoc++’s performance stems from robust tree-level correspondences in Fig. 14, which remain reliable under partial overlap and enable centimeter-level accuracy comparable to point-based registration methods, as detailed in Appendix C.

C. Inter-session Place Recognition

The previous three experiments focused exclusively on performance within intra-session settings. We now extend our evaluation to inter-session scenarios with larger temporal gaps, analyzing the robustness of the proposed method under more challenging long-term environmental changes.

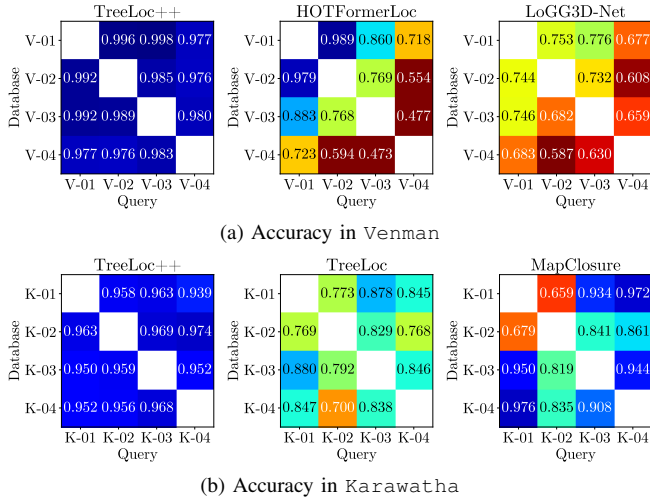


FIGURE 16: (**Exp C**) Accuracy matrix for inter-session place recognition. Blue tones indicate higher accuracy, while red tones denote lower accuracy. TreeLoc++ shows the most reliable performance across all session pairs.

We aim to determine whether methods maintain consistent performance under seasonal and structural variation.

Evaluation protocol: TreeLoc++ was evaluated in an inter-session setting using the local inventory mode on Venman01–04 and Karawatha01–04. Learning-based methods were trained on Wild-Places, following the official protocol, which restricts evaluation to predefined regions, as shown in Fig. 15. To quantitatively assess robustness across sessions, we introduce a Stability Ratio, $S = \log(\mu/(\sigma + \epsilon))$, where μ and σ denote the mean and standard deviation of the performance metric over the 12 inter-session pairs, and ϵ is a small constant for numerical stability. Unlike raw variance, this ratio favors methods that are both high-performing and consistent.

TreeLoc++: As reported in Table. 5, TreeLoc++ achieved the highest mean performance and Stability Ratio on most metrics. Even when learning-based models were trained on the same dataset, TreeLoc++ surpassed them in both mean performance and stability, ranking second only in R@1 on Venman. On Karawatha, recall decreased in open areas with fewer distinctive vertical structures; nevertheless, TreeLoc++ achieved Stability Ratio comparable to or higher than several learning-based methods.

Baselines: Most hand-crafted methods degraded in the inter-session setting, indicating limited robustness to temporal variation. While TreeLoc outperformed other hand-crafted baselines, it still lagged behind learning-based methods. Among learning-based approaches, LoGG3D-Net and HOTFormerLoc achieved the highest mean performance; however, LoGG3D-Net degraded on Venman, and HOTFormerLoc’s low Stability Ratios suggest inconsistent performance across sessions. As shown in Fig. 15, LoGG3D-Net produced frequent mismatches, and HOTFormerLoc deteriorated with increasing temporal gaps. Furthermore, while these methods still retrieve true positives via minimum descriptor dis-

tance, accompanying false positives necessitate an appropriate threshold to filter out incorrect matches.

Fixed-threshold transfer: Consequently, we assessed inter-session robustness using fixed-threshold accuracy analysis in Fig. 16. To reflect realistic deployment where thresholds cannot be returned for each session pair, we fixed a single operating threshold per method by maximizing F1 score on 01–02 pair, and applied it unchanged to all remaining pairs.

As shown in Fig. 16a and Fig. 16b, TreeLoc++ was the only method that consistently achieved high accuracy across all pairs. In contrast, baseline methods exhibited large fluctuations. HOTFormerLoc and LoGG3D-Net degraded substantially on Venman04 due to pronounced environmental changes. Conversely, MapClosure and TreeLoc performed poorly on Karawatha01–02 because low thresholds admitted many false positives, but improved in later sessions where larger appearance differences made discrimination easier. Overall, these results suggest that the similarity scores used by the baselines are brittle under fixed thresholds. In contrast, the proposed overlap score $\mathcal{O}(Q, C)$ maintains stable separation between true and false matches, demonstrating robust performance without session-specific tuning.

D. Multi-session Metric Localization with Global DFIs

This experiment assesses the feasibility of using multiple global forest inventories to localize incoming trajectories using local observations in a scalable and robust way.

Evaluation protocol: We evaluated relocalization against a pre-built global forest inventory that serves as a persistent reference map. Query frames were processed in local inventory mode, while the database consisted of a single global inventory. To cover the spatial extent of the reference map, we constructed database entries at 5 m intervals in the horizontal plane as shown in Fig. 17a. At each sampled location, a local inventory was formed by extracting nearby trees, and the corresponding TreeLoc++ descriptor was stored in the global descriptor database. Experiments were conducted on Evo23:00–03, Evo25:00, 02, 03, 05, and Venman01–02. For each sequence, initial odometry was obtained using GeoTransformer [72]. We first generated intra-session constraints using local inventories, and then incrementally added inter-session constraints by matching queries to the global descriptor database.

Constraint selection differed by method. Baseline constraints were selected either by (i) ground truth-validated success (SR) or (ii) a confidence threshold chosen to maximize F1 from intra-session localization. For TreeLoc and TreeLoc++, we used a fixed threshold, $\mathcal{O}(Q, C) > 0.2$. To ensure a sufficient number of constraints under the SR-based setting, we relaxed the true-positive distance threshold to 10 m. All selected constraints were optimized using GTSAM. Trajectory accuracy was evaluated with the Evo toolkit [73] using ATE and ARE. Except for intra-session loop evaluations, we report results without applying SE(3) alignment during Evo evaluation. We additionally report the

TABLE 6: (Exp D) Global relocalization results, where loop closure and inter-session constraints are added incrementally from additional sequences.

Metrics	LoGG3D-Net		BTC		MapClosure		TreeLoc	TreeLoc++
	SR	F1	SR	F1	SR	F1	$\mathcal{O} > 0.2$	
+ Loop								
Size	1.2 MB		44MB		2.6 MB		227.9 KB	
# Const.	16	55	5	14	1	1	33	38
ATE [m]	0.35	10.40	0.37	<i>0.31</i>	0.46	0.46	0.31	0.32
ARE [°]	1.53	45.61	1.63	1.33	1.96	1.96	<i>1.49</i>	1.53
+ 25:02								
Size	3.7 MB		90.8 MB		7.7 MB		11.2 KB	
# Const.	0	29	0	0	0	25	2	58
ATE [m]	33.73	20.60	33.80	33.78	34.05	15.20	<i>10.21</i>	0.57
ARE [°]	41.58	63.96	42.20	41.52	42.48	24.36	<i>7.93</i>	1.75
+ 25:03								
Size	2.0 MB		20.2 MB		2.9 MB		5.9 KB	
# Const.	0	17	0	1	0	15	7	24
ATE [m]	33.73	19.35	33.80	23.97	34.05	11.50	<i>2.74</i>	0.60
ARE [°]	41.58	53.14	42.20	26.64	42.48	37.06	<i>7.05</i>	1.92
+ 25:05								
Size	3.9 MB		74MB		7.3 MB		14.9 KB	
# Const.	0	1	0	0	0	6	3	25
ATE [m]	33.73	18.66	33.80	23.97	34.05	25.93	<i>1.96</i>	0.53
ARE [°]	41.58	51.55	42.20	26.64	42.48	80.74	<i>3.49</i>	1.91
V-01								
Size	11.3 MB		1.60 GB		21.7 MB		3.2 MB	
# Const.	314	1400	61	0	84	336	273	338
ATE [m]	6.74	174.78	7.18	175.88	6.88	7.95	<i>7.53</i>	6.76
ARE [°]	2.94	71.39	3.06	66.90	2.96	3.52	3.36	2.92
+ V-02								
Size	54.1 MB		2.00 GB		130.5 MB		68.7 KB	
# Const.	217	1451	6	46	0	19	69	602
ATE [m]	1.72	146.71	2.90	295.14	23.60	104.68	<i>5.47</i>	1.23
ARE [°]	0.99	52.05	1.56	81.21	5.00	75.77	<i>2.25</i>	1.13

• Size denotes the storage required for the descriptors and forest inventories.
 • # Const. reports the number of selected constraints used in trajectory optimization.

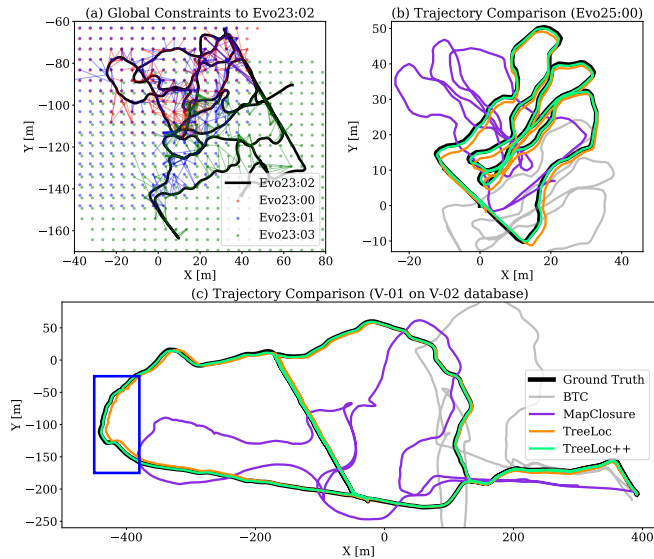


FIGURE 17: (Exp D) Relocalization against a global forest inventory. (a) A global descriptor database is built by querying the global inventory at uniformly sampled poses on a 5 m grid, efficiently covering the full map extent. (b-c) Using the relocalization constraints to shift trajectories into the global frame, TreeLoc++ produces trajectories closest to the ground truth.

number of constraints produced by each method, as well as the storage required for descriptors and forest inventories.

Relocalization accuracy: As reported in Table. 6, TreeLoc++ achieved the lowest trajectory error in nearly all settings by correcting raw odometry with accurate and reliable constraints. Even when baselines were restricted to SR-validated constraints, TreeLoc++ typically attained lower or

comparable error by leveraging a larger set of accurate constraints. When baselines used F1-based thresholds, the number of selected constraints increased due to false positives, substantially degrading trajectory accuracy. Overall, these results indicate that threshold-based constraint selection in existing methods is brittle in practical global relocalization, consistent with observations in earlier sections.

Fig. 17a illustrates $Evo_{23:02}$, where TreeLoc++ aligned the trajectory to the global reference frame by incorporating constraints from three inter-session sequences. As shown in Fig. 17b-c, the optimized trajectories closely match the ground truth, benefiting from consistent and accurate constraints. On Venman, which contains 6,918 database entries, TreeLoc++ demonstrated its reliability by efficiently querying the large-scale global database and aligning all trajectories into a common world frame.

Storage and scalability: TreeLoc++ also offers clear storage advantages. Compared to other descriptor-based methods, it requires substantially less storage due to its compact representation. Although the Loop configuration stores a local inventory per pose, the total storage remains on the megabyte scale, and the global inventory is even smaller, as shown in Table. 6. These results show that TreeLoc++ supports accurate and scalable global trajectory estimation with minimal storage overhead.

E. Multi-session Registration with Global DFIs

In this section, we seek to address the following question: whether global forest inventories alone are sufficient for accurate map-to-map registration across sessions, in the absence of raw point clouds or GNSS.

Evaluation protocol: This section evaluates map-to-map registration using only global forest inventories, without relying on raw point clouds. For each session, a single global forest inventory served as the map representation. System poses were sampled along each session, and at each sampled pose, nearby trees were extracted from the global inventory to form pose-centric inventories. TreeLoc++ descriptors were computed for these samples and matched across all session pairs to establish inter-session constraints, using a fixed overlap threshold of $\mathcal{O}(Q, C) > 0.2$.

TreeLoc++: Fig. 18 illustrates the initial and aligned trajectories of $Evo_{25:00-08}$, along with a combined point-cloud visualization obtained by transforming scans using the aligned poses. Thanks to TreeLoc++’s high localization accuracy, trunk structures align consistently across sessions, even though raw point clouds are not used for constraint generation or registration.

GNSS and point-cloud baselines: For comparison, we performed multi-session alignment using GNSS by estimating a rigid transform between each session’s local trajectory and its GNSS-referenced trajectory. As shown for $Evo_{25:08}$ (green), this produced noticeable misalignments and inconsistent trajectories across sessions, indicating that GNSS provides only coarse alignment and lacks the precision needed

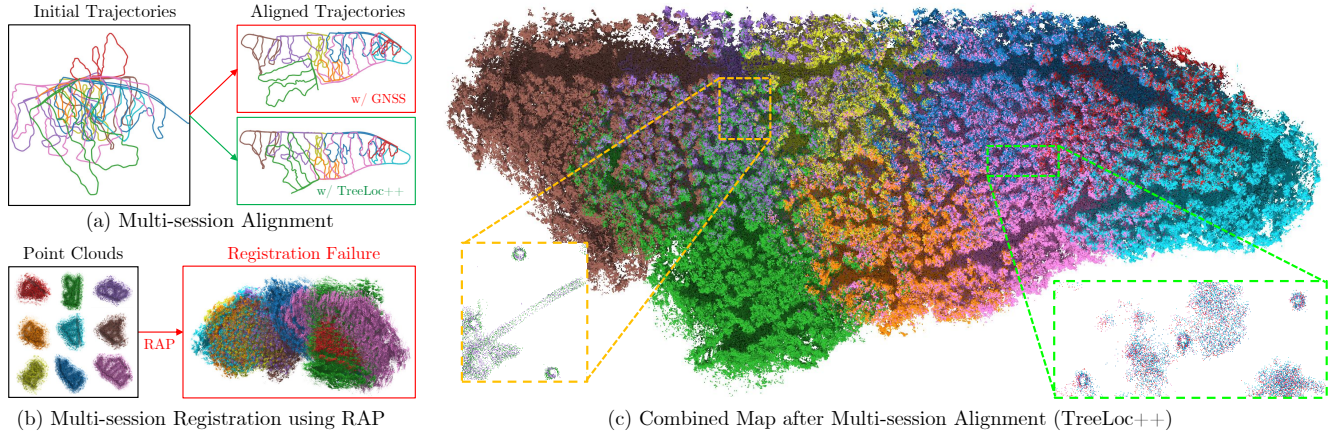


FIGURE 18: (Exp E) Multi-session alignment results. (a) Each session trajectory is expressed in its own local frame, with all trajectories starting at the origin; GNSS-based alignment remains inconsistent across sessions, with clear misalignment in the green trajectory, whereas TreeLoc++ yields more accurate multi-session alignment. (b) Point cloud-based multi-session registration fails in repetitive forest environments due to ambiguous geometry. (c) Combined map generated using TreeLoc++ aligned poses, where the zoomed view highlights consistent alignment of tree trunks and fallen trees observed across multiple sessions, demonstrating accurate alignment.

for stem-level consistency in forests. We further compared against RAP [74], a point cloud-based registration baseline, as shown in Fig. 18b. In the unstructured and repetitive forest geometry, RAP failed to converge to a correct alignment, resulting in substantial registration errors.

Long-term scalability: Finally, Fig. 1 shows large-scale alignment across all 15 sessions from $E_{v023:00-05}$ and $E_{v025:00-08}$. Despite a two-year gap and different LiDAR FoVs (104° in 2025 vs. 31° in 2023), TreeLoc++ aligned all sessions using only the global forest inventory, with a total map size of 250 KB. These results highlight the robustness of TreeLoc++ and demonstrate that lightweight, geometry-based inventories support scalable multi-session registration, enabling consistent inventory maintenance and long-term ecological monitoring as detailed in Appendix D.

F. Robustness and Efficiency Analysis

1) Viewpoint Robustness

Evaluation Protocol: We evaluated the rotation invariance of TreeLoc++ using Venman02 as the database and Venman03 as the query. To simulate viewpoint variation, we applied synthetic rotations to the database point clouds and DFIs. Yaw was varied from -180° to 180° in 30° steps, and roll and pitch were jointly varied from -90° to 90° in 15° steps. For each augmented database, we measured R@1 and quantified consistency via the Stability Ratio (S).

Results: As shown in Table. 7 and Fig. 19, all methods except TreeLoc++ failed under roll-pitch perturbations, despite remaining stable under yaw. MapClosure showed partial robustness to small tilts, but its accuracy deteriorated as perturbations increased. In contrast, TreeLoc++ maintained high R@1 across all rotations, enabled by yaw-invariant TDH/PDH and 2D triangles, and axis-based alignment that stabilizes projections under tilt. These results confirm TreeLoc++’s robustness to severe viewpoint variations.

TABLE 7: (Exp F-1) Invariance analysis across different orientation

Methods	Yaw (13 pairs)			Roll & Pitch (13 pairs)			Full Rot. (169 pairs)		
	Mean	σ	S	Mean	σ	S	Mean	σ	S
MapClosure	0.363	0.002	2.281	0.273	0.132	0.316	0.281	0.130	0.336
LoGG3D-Net	0.664	0.002	2.592	0.168	0.258	-0.186	0.166	0.252	-0.181
HOTFormerLoc	0.385	0.361	0.028	0.191	0.288	-0.179	0.109	0.196	-0.255
TreeLoc++	0.951	0.001	3.024	0.952	0.001	3.075	0.952	0.001	3.200

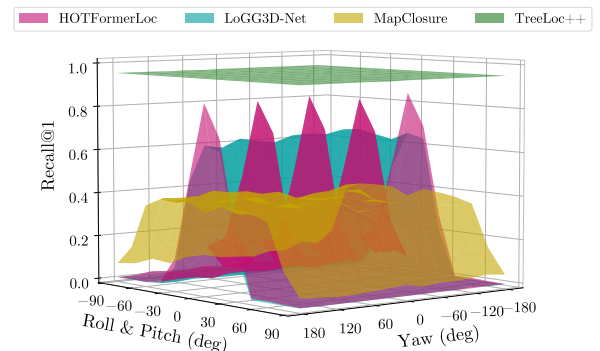


FIGURE 19: (Exp F-1) R@1 performance with different orientation

2) Runtime Efficiency

Evaluation Protocol: We conducted two experiments to analyze runtime. First, we reported the total inter-session localization time, including place recognition and pose estimation (geometric verification). To compare localization efficiency across methods, we followed the large-scale setup from §D, using 6,918 database entries and 1,451 queries. Second, to analyze TreeLoc++ in detail, we used Karawatha03 to measure the runtime of descriptor generation, place recognition, and pose estimation separately. For a fair comparison, we evaluated only methods with publicly available C++ implementations on an 11th Gen Intel Core i7-11700 @ 2.50 GHz and an NVIDIA GeForce RTX 3080 GPU.

Results: As shown in Table. 8, TreeLoc++ achieved the lowest runtime among all methods. BTC incurred high runtime due to costly triangle-wise comparisons during place

TABLE 8: (Exp F-2) Total runtime for all queries on large databases [s]

Method	Place Recognition	Pose Estimation	Total Time
BTC	382.29	10.49	392.78
MapClosure	5.60	4.46	10.06
TreeLoc++	2.98	3.43	6.41

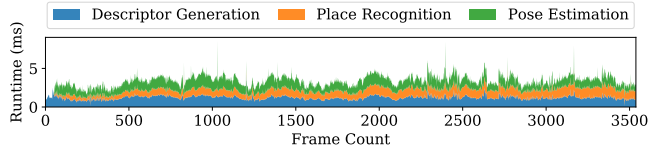


FIGURE 20: (Exp F-2) Runtime for Intra-session localization in K-03

recognition, while MapClosure was faster by leveraging lightweight ORB-based image matching. TreeLoc++ outperformed both by avoiding per-candidate geometric checks and limiting pose estimation to a small set of top-ranked matches. As shown in Fig. 20, TreeLoc++ also benefits from fast descriptor generation via DFI, requiring less than 1 ms per query. This makes on-demand descriptor computation nearly as efficient as preloading, avoiding additional I/O cost and storage. Moreover, TreeLoc++ maintains low runtime as the database grows, due to efficient filtering using TDH and PDH. Although histogram distance computations grow with the database size, the increase remains small thanks to the low-dimensional histogram. These design choices enable TreeLoc++ to support fast localization while conserving compute for downstream tasks like mapping and planning.

G. Ablation Studies

The contribution of each TreeLoc++ component was analyzed through an ablation study. Experiments were conducted on two contrasting environments: the small-scale Stein am Rhein and the large-scale Karawatha03.

1) Ablation on Coarse Retrieval with TDH and PDH

Evaluation Protocol: We assessed the impact of TDH and PDH by incrementally enabling each component and measuring candidate retrieval performance. We report R@1 and R@50, the average number of true positives in the retrieved candidate set, and the false negative rate (FNR), defined as the fraction of queries for which the ground truth match is absent from the retrieved candidates.

Results: As shown in Table. 9, Stein am Rhein exhibited only minor changes in recall, since its limited spatial extent already yields many true positives in coarse retrieval. However, combining TDH and PDH increased true positives and reduced the FNR. On the larger Karawatha03, this combination substantially improved both recall and FNR. Fig. 21 also confirms that the dual histogram design boosts true positives across varying candidate counts. When using only triangle descriptors without histograms, geometrically similar but distant triangles frequently collide in the hash space, causing false scene matches. In contrast, combining histograms stabilizes retrieval by jointly encoding inter-tree

TABLE 9: (Exp G-1) Ablation studies on TDH and PDH

Config.		Stein am Rhein				Karawatha03			
TDH	PDH	# TP	FNR	R@1	R@50	# TP	FNR	R@1	R@50
✗	✗	-	-	0.939	0.935	-	-	0.820	0.845
✓	✗	15.069	0.024	0.933	0.943	3.852	0.063	0.834	0.863
✗	✓	16.701	0.022	0.939	0.933	3.771	0.076	0.817	0.845
✓	✓	17.016	0.020	0.941	0.939	4.662	0.038	0.864	0.874

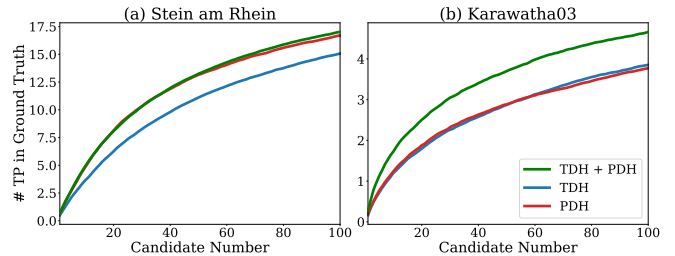


FIGURE 21: (Exp G-1) Number of true positives per candidate count

relationships and location-centered distributions, providing complementary cues for robust candidate selection.

2) Ablation on Candidate Re-ranking and Outlier Rejection

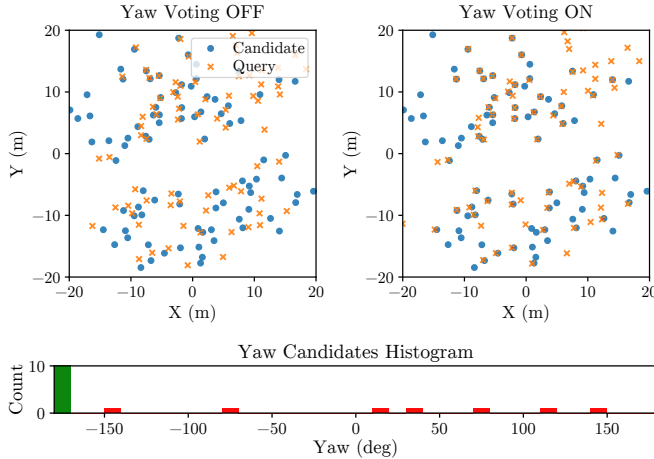
Evaluation Protocol: We evaluated three refinement strategies: the translation penalty, yaw voting, and DBH filtering. Since these components influence both place recognition and metric localization, we report R@1, AUC, R@50, and SR. **Results:** As shown in Table. 10, enabling the translation penalty improved R@1, AUC, and SR, while R@50 changed only marginally. By promoting spatially adjacent candidates, it increased R@1, and this led to more accurate overlap scoring, resulting in higher AUC. The number of correctly retrieved true positives also increased, which raised the SR. Yaw voting and DBH filtering further improved performance by suppressing outlier triangle correspondences, leading to more accurate scoring and correspondence selection. These gains were more pronounced on Karawatha03, where the large inventory generated a significant number of triangles, making the matching stage more prone to outliers. Fig. 22a illustrates that yaw voting enables more reliable pose estimation on Karawatha03; despite the presence of outlier correspondences, it selects a consistent inlier set around the dominant yaw, improving query-candidate alignment. DBH filtering further improves performance when applied after yaw voting by removing residual outliers that yaw voting alone cannot suppress. As shown in Fig. 22b, these outliers otherwise lead to inaccurate pose estimation, whereas DBH filtering yields more consistent correspondences.

3) Ablation on TreeLoc++ Extensions over TreeLoc

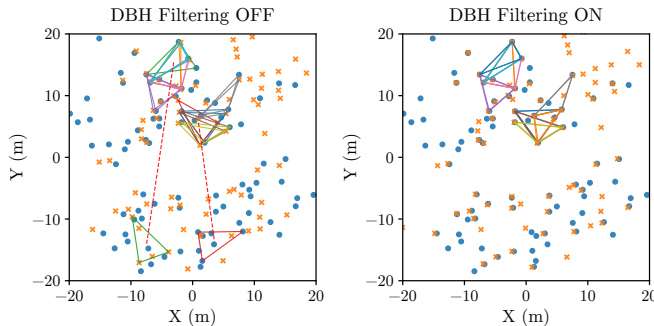
Evaluation Protocol: We evaluated three extensions in TreeLoc++ over TreeLoc: reusing preceding inventories to increase the number of trees, planar alignment via IRLS, and vertical correction for full 6-DoF pose refinement. Their impact was quantified using R@1, R@50, ATE, and ARE.

TABLE 10: (Exp G-2) Ablation studies on refinements

Refinement			Stein am Rhein				Karawatha03			
Pen.	Vot.	Filt.	R@1	AUC	R@50	SR	R@1	AUC	R@50	SR
✗	✗	✗	0.902	0.983	0.933	0.872	0.644	0.825	0.809	0.577
✓	✗	✗	0.927	0.998	0.935	0.894	0.803	0.995	0.808	0.730
✓	✓	✗	0.933	0.998	0.939	0.902	0.852	0.998	0.850	0.796
✓	✓	✓	0.941	0.998	0.939	0.906	0.864	0.998	0.874	0.816



(a) Effect of Yaw Voting in Karawatha03



(b) Effect of DBH Filtering in Karawatha03

FIGURE 22: (Exp G-2) Ablation of yaw voting and DBH filtering. (a) Registration with yaw voting disabled and enabled, where a histogram built from triangle matches suppresses orientation outliers by selecting the dominant yaw, improving query-candidate alignment. (b) 10 triangle matches with DBH filtering disabled and enabled; consistent colors indicate corresponding pairs. Without DBH filtering, outlier pairs (red dashed) remain and degrade pose estimation, while DBH filtering removes them.

Results: As shown in Table. 11, reusing preceding windows had little effect on Stein am Rhein, where most frames already contain sufficient tree observations. In contrast, in open or sparse areas of Karawatha03, this reuse increased the number of matched triangles, improving recall. IRLS refinement was particularly effective in occluded or sparsely observed scenes. When tree centers were inconsistently estimated, IRLS stabilized the 2D alignment around the initial estimate, producing more consistent correspondences and improved recall. While these two strategies mainly improved retrieval, their impact on ATE and ARE was limited because the pose refinement stage was unchanged.

TABLE 11: (Exp G-3) Ablation studies on system components

System Components			Stein am Rhein				Karawatha03			
Reuse	IRLS	Corr.	R@1	R@50	ATE	ARE	R@1	R@50	ATE	ARE
✗	✗	✗	0.939	0.915	0.152	1.331	0.825	0.844	0.099	0.730
✓	✗	✗	0.939	0.921	0.154	1.356	0.852	0.852	0.101	0.737
✓	✓	✗	0.941	0.927	0.149	1.359	0.864	0.871	0.103	0.751
✓	✓	✓	0.941	0.939	0.087	0.470	0.864	0.874	0.080	0.260

In contrast, vertical correction significantly reduced ATE and ARE by jointly optimizing roll, pitch, and height, enabling accurate 6-DoF localization without degrading recall.

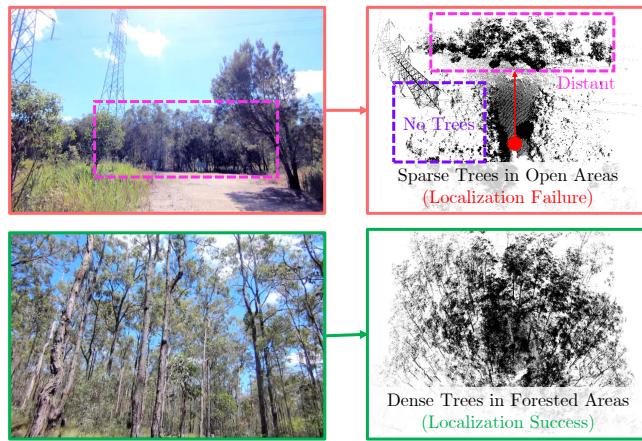
VI. Limitations of TreeLoc++

Failure Cases in Open Areas: TreeLoc++ performance varies significantly between the open areas and deep-forest regions. In the open areas of Karawatha03, tree observations tend to be sparse and distant, providing insufficient geometric constraints for robust localization as shown in Fig. 23a. This often leads to degraded downstream pose estimation. However, in deep forests, the density of nearby trunks allows the system to achieve highly successful localization through stable correspondences. While TreeLoc++ is environment-dependent, it naturally complements GNSS: open areas typically offer strong GNSS reception thanks to the lack of canopy obstruction, whereas dense forests provide richer geometric features for reliable localization when GNSS becomes unreliable. This suggests a practical deployment strategy that uses GNSS in open areas and switches to TreeLoc++ as tree density increases.

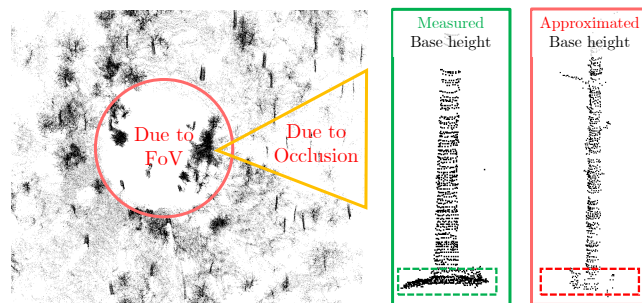
Inaccurate Base Height under Terrain Occlusion: TreeLoc++ relies on estimated base heights for full 6-DoF alignment, so base height errors can destabilize roll, pitch, and height refinement. As shown in Fig. 23b, this occurs when limited sensor FoV or severe occlusions prevent sufficient terrain observations around a tree. In such cases, the base height must be approximated from nearby data, which can deviate from the true value. This issue is more pronounced in local inventory mode due to limited payload coverage. In contrast, global inventory mode mitigates it by leveraging all explored payloads during tree reconstruction, providing broader multi-view coverage for base height estimation. Nevertheless, the practical impact is marginal: the error increase from 3-DoF to 6-DoF alignment remains at the centimeter level with stable rotation error. Furthermore, RANSAC-based filtering effectively rejects base height outliers, as supported by results in Table. 4 and Appendix E.

VII. Conclusion

This paper presented TreeLoc++, a global localization framework for forest environments based on DFIs that eliminates the need to store raw point clouds. TreeLoc++ builds local and global inventories by reconstructing tree instances from aggregated payloads. For localization, it performs stem-axis-based alignment and 2D projection, and retrieves candidates via a coarse-to-fine matching strategy, starting with TDH and



(a) Examples of Localization Failure and Success across Different Areas



(b) Inaccurate Base Height from FoV and Occlusion

FIGURE 23: Limitations of TreeLoc++. (a) Sparse and distant tree observations in open areas provide insufficient geometric constraints, leading to failure. In contrast, dense forests enable successful localization through abundant correspondences. (b) Limited sensor FoV and occlusions prevent direct ground measurements, requiring an approximation of the base height that may introduce errors relative to the true base height.

PDH, and 2D triangle descriptor for efficient retrieval. It then rejects outliers through DBH filtering and yaw-consistent inlier voting, and refines the 6-DoF pose through geometric verification with constrained optimization of roll, pitch, and height. We evaluated TreeLoc++ on 27 sequences from three datasets, including multi-session data collected two years apart. The results demonstrate robust place recognition and centimeter-level localization accuracy, while maintaining a compact map representation of just 250 KB across 15 sessions covering 7.98 km trajectories. TreeLoc++ outperformed both hand-crafted and learning-based baselines in accuracy and achieved the lowest runtime. Ablation studies further confirmed that each proposed component contributes to the overall performance and robustness. Future work will focus on inventory construction. Although TreeLoc++ is accurate and efficient, the current pipeline relies on individual tree segmentation and forest inventory generation (using RealtimeTrees), which requires aggregating point cloud payloads. With improvements to DFI construction in the future, we would envisage TreeLoc++ achieving further gains in localization performance.

REFERENCES

- [1] H. Yin, X. Xu, S. Lu, X. Chen, R. Xiong, S. Shen, C. Stachniss, and Y. Wang, "A survey on global lidar localization: Challenges, advances and open problems," *Intl. J. of Comput. Vision*, vol. 132, no. 8, pp. 3139–3171, 2024.
- [2] M. Miettinen, M. Ohman, A. Visala, and P. Forsman, "Simultaneous localization and mapping for forest harvesters," in *Proc. IEEE Intl. Conf. on Robot. and Automat.*, 2007, pp. 517–522.
- [3] M. Mattamala, J. Frey, P. Libera, N. Chebrolu, G. Martius, C. Cadena, M. Hutter, and M. Fallon, "Wild visual navigation: Fast traversability learning via pre-trained models and online self-supervision," *Autonomous Robots*, vol. 49, no. 3, p. 19, 2025.
- [4] M. Mattamala, N. Chebrolu, J. Frey, L. Freimuth, H. Oh, B. Casseau, M. Hutter, and M. Fallon, "Building forest inventories with autonomous legged robots—system, lessons, and challenges ahead," *arXiv preprint arXiv:2506.20315*, 2025.
- [5] X. Liang, V. Kankare, J. Hyyp, Y. Wang, A. Kukko, H. Haggren, X. Yu, H. Kaartinen, A. Jaakkola, F. Guan *et al.*, "Terrestrial laser scanning in forest inventories," *ISPRS J. Photogramm. Remote Sensing*, vol. 115, pp. 63–77, 2016.
- [6] M. Pierzchała, P. Gigure, and R. Astrup, "Mapping forests using an unmanned ground vehicle with 3d lidar and graph-slam," *Comput. Elec. Agric.*, vol. 145, pp. 217–225, 2018.
- [7] S. W. Chen, G. V. Nardari, E. S. Lee, C. Qu, X. Liu, R. A. F. Romero, and V. Kumar, "Sloam: Semantic lidar odometry and mapping for forest inventory," *IEEE Robot. and Automat. Lett.*, vol. 5, no. 2, pp. 612–619, 2020.
- [8] X. Liu, G. V. Nardari, F. Cladera, Y. Tao, A. Zhou, T. Donnelly, C. Qu, S. W. Chen, R. A. Romero, C. J. Taylor *et al.*, "Large-scale autonomous flight with real-time semantic slam under dense forest canopy," *IEEE Robot. and Automat. Lett.*, vol. 7, no. 2, pp. 5512–5519, 2022.
- [9] R. Valbuena, F. Mauro, R. Rodriguez-Solano, and J. Manzanera, "Accuracy and precision of gps receivers under forest canopies in a mountainous environment," *Spanish journal of agricultural research*, vol. 8, no. 4, pp. 1047–1057, 2010.
- [10] I.-S. Lee and L. Ge, "The performance of rtk-gps for surveying under challenging environmental conditions," *Earth, planets and space*, vol. 58, no. 5, pp. 515–522, 2006.
- [11] M. Dassot, T. Constant, and M. Fournier, "The use of terrestrial lidar technology in forest science: application fields, benefits and challenges," *Annals of forest science*, vol. 68, no. 5, pp. 959–974, 2011.
- [12] H.-M. Cho, J.-H. Oh, J.-W. Park, Y.-S. Choi, J.-S. Lee, and S.-K. Han, "Application of real-time positioning systems to a forest stand for precision forest management," *Sensors & Materials*, vol. 34, 2022.
- [13] M. A. Wulder, C. W. Bater, N. C. Coops, T. Hilker, and J. C. White, "The role of lidar in sustainable forest management," *The forestry chronicle*, vol. 84, no. 6, pp. 807–826, 2008.
- [14] G. Kim and A. Kim, "Scan context: Egocentric spatial descriptor for place recognition within 3d point cloud map," in *Proc. IEEE/RSJ Intl. Conf. on Intell. Robots and Sys.*, 2018, pp. 4802–4809.
- [15] G. Kim, S. Choi, and A. Kim, "Scan context++: Structural place recognition robust to rotation and lateral variations in urban environments," *IEEE Trans. Robot.*, vol. 38, no. 3, pp. 1856–1874, 2021.

- [16] H. Kim, J. Choi, T. Sim, G. Kim, and Y. Cho, "Narrowing your fov with solid: Spatially organized and lightweight global descriptor for fov-constrained lidar place recognition," *IEEE Robot. and Automat. Lett.*, 2024.
- [17] C. Yuan, J. Lin, Z. Zou, X. Hong, and F. Zhang, "Std: Stable triangle descriptor for 3d place recognition," in *Proc. IEEE Intl. Conf. on Robot. and Automat.*, 2023, pp. 1897–1903.
- [18] C. Yuan, J. Lin, Z. Liu, H. Wei, X. Hong, and F. Zhang, "Btc: A binary and triangle combined descriptor for 3-d place recognition," *IEEE Trans. Robot.*, vol. 40, pp. 1580–1599, 2024.
- [19] S. Gupta, T. Guadagnino, B. Mersch, I. Vizzo, and C. Stachniss, "Effectively detecting loop closures using point cloud density maps," in *Proc. IEEE Intl. Conf. on Robot. and Automat.*, 2024, pp. 10260–10266.
- [20] H. Yang, J. Shi, and L. Carlone, "Teaser: Fast and certifiable point cloud registration," *IEEE Trans. Robot.*, vol. 37, no. 2, pp. 314–333, 2020.
- [21] H. Lim, S. Yeon, S. Ryu, Y. Lee, Y. Kim, J. Yun, E. Jung, D. Lee, and H. Myung, "A single correspondence is enough: Robust global registration to avoid degeneracy in urban environments," in *Proc. IEEE Intl. Conf. on Robot. and Automat.*, 2022, pp. 8010–8017.
- [22] H. Lim, D. Kim, G. Shin, J. Shi, I. Vizzo, H. Myung, J. Park, and L. Carlone, "Kiss-matcher: Fast and robust point cloud registration revisited," in *Proc. IEEE Intl. Conf. on Robot. and Automat.*, 2025, pp. 11104–11111.
- [23] H. Oh, N. Chebrolu, M. Mattamala, L. Freißmuth, and M. Fallon, "Evaluation and deployment of lidar-based place recognition in dense forests," in *Proc. IEEE/RSJ Intl. Conf. on Intell. Robots and Sys.*, 2024, pp. 12824–12831.
- [24] L. Li, X. Kong, X. Zhao, T. Huang, W. Li, F. Wen, H. Zhang, and Y. Liu, "Ssc: Semantic scan context for large-scale place recognition," in *Proc. IEEE/RSJ Intl. Conf. on Intell. Robots and Sys.*, 2021, pp. 2092–2099.
- [25] R. Dubé, D. Dugas, E. Stumm, J. Nieto, R. Siegwart, and C. Cadena, "Segmatch: Segment based place recognition in 3d point clouds," in *Proc. IEEE Intl. Conf. on Robot. and Automat.*, 2017, pp. 5266–5272.
- [26] K. Vidanapathirana, J. Knights, S. Hausler, M. Cox, M. Ramezani, J. Jooste, E. Griffiths, S. Mohamed, S. Sridharan, C. Fookes *et al.*, "Wildscenes: A benchmark for 2d and 3d semantic segmentation in large-scale natural environments," *Intl. J. of Robot. Research*, vol. 44, no. 4, pp. 532–549, 2025.
- [27] G. Tinchev, A. Penate-Sanchez, and M. Fallon, "Learning to see the wood for the trees: Deep laser localization in urban and natural environments on a cpu," *IEEE Robot. and Automat. Lett.*, vol. 4, no. 2, pp. 1327–1334, 2019.
- [28] G. Tinchev, S. Nobili, and M. Fallon, "Seeing the wood for the trees: Reliable localization in urban and natural environments," in *Proc. IEEE/RSJ Intl. Conf. on Intell. Robots and Sys.*, 2018, pp. 8239–8246.
- [29] M. Jung, N. Chebrolu, L. C. de Lima, H. Oh, M. Fallon, and A. Kim, "Treeloc: 6-dof lidar global localization in forests via inter-tree geometric matching," *arXiv preprint arXiv:2602.01501*, 2026.
- [30] C. J. Gleason and J. Im, "Forest biomass estimation from airborne lidar data using machine learning approaches," *Remote Sensing of Environment*, vol. 125, pp. 80–91, 2012.
- [31] W. Li, Q. Guo, M. K. Jakubowski, M. Kelly *et al.*, "A new method for segmenting individual trees from the lidar point cloud," *Photogrammetric Engineering and Remote Sensing*, vol. 78, no. 1, pp. 75–84, 2012.
- [32] L. Wallace, A. Lucieer, and C. S. Watson, "Evaluating tree detection and segmentation routines on very high resolution uav lidar data," *IEEE Trans. Geosci. and Remote Sensing*, vol. 52, no. 12, pp. 7619–7628, 2014.
- [33] K. Itakura, S. Miyatani, and F. Hosoi, "Estimating tree structural parameters via automatic tree segmentation from lidar point cloud data," *IEEE J. of Selected Topics in Applied Earth Observations and Remote Sensing*, vol. 15, pp. 555–564, 2021.
- [34] M. V. Malladi, T. Guadagnino, L. Lobefaro, M. Mattamala, H. Griess, J. Schweier, N. Chebrolu, M. Fallon, J. Behley, and C. Stachniss, "Tree instance segmentation and traits estimation for forestry environments exploiting lidar data collected by mobile robots," in *Proc. IEEE Intl. Conf. on Robot. and Automat.*, 2024, pp. 17933–17940.
- [35] L. Freißmuth, M. Mattamala, N. Chebrolu, S. Schaefer, S. Leutenegger, and M. Fallon, "Online tree reconstruction and forest inventory on a mobile robotic system," in *Proc. IEEE/RSJ Intl. Conf. on Intell. Robots and Sys.*, 2024, pp. 11765–11772.
- [36] C. R. Qi, L. Yi, H. Su, and L. J. Guibas, "Pointnet++: Deep hierarchical feature learning on point sets in a metric space," *Advances in neural information processing systems*, vol. 30, 2017.
- [37] Q. Hu, B. Yang, L. Xie, S. Rosa, Y. Guo, Z. Wang, N. Trigoni, and A. Markham, "Randla-net: Efficient semantic segmentation of large-scale point clouds," in *Proc. IEEE Conf. on Comput. Vision and Pattern Recog.*, 2020, pp. 11108–11117.
- [38] M. V. Malladi, N. Chebrolu, I. Scacchetti, L. Lobefaro, T. Guadagnino, B. Casseau, H. Oh, L. Freißmuth, M. Karppinen, J. Schweier *et al.*, "Digiforests: a longitudinal lidar dataset for forestry robotics," in *Proc. IEEE Intl. Conf. on Robot. and Automat.*, 2025, pp. 1459–1466.
- [39] J. Knights, K. Vidanapathirana, M. Ramezani, S. Sridharan, C. Fookes, and P. Moghadam, "Wild-places: A large-scale dataset for lidar place recognition in unstructured natural environments," in *Proc. IEEE Intl. Conf. on Robot. and Automat.*, 2023, pp. 11322–11328.
- [40] B. N. Bailey and M. H. Ochoa, "Semi-direct tree reconstruction using terrestrial lidar point cloud data," *Remote Sensing of Environment*, vol. 208, pp. 133–144, 2018.
- [41] M. Hussein, K. Iagnemma, and M. Renner, "Global localization of autonomous robots in forest environments," *Photogrammetric Engineering & Remote Sensing*, vol. 81, no. 11, pp. 839–846, 2015.
- [42] X. Xu, S. C. Lu, J. Wu, H. Lu, Q. Zhu, Y. Liao, R. Xiong, and Y. Wang, "Ring++: Roto-translation invariant gram for global localization on a sparse scan map," *IEEE Trans. Robot.*, vol. 39, no. 6, pp. 4616–4635, 2023.
- [43] L. He, X. Wang, and H. Zhang, "M2dp: A novel 3d point cloud descriptor and its application in loop closure detection," in *Proc. IEEE/RSJ Intl. Conf. on Intell. Robots and Sys.*, 2016, pp. 231–237.
- [44] S. C. Lu, X. Xu, H. Yin, Z. Chen, R. Xiong, and Y. Wang, "One ring to rule them all: Radon sinogram for place recognition, orientation and translation estimation," in *Proc. IEEE/RSJ Intl. Conf. on Intell. Robots and Sys.*, 2022, pp. 2778–2785.
- [45] R. B. Rusu, N. Blodow, and M. Beetz, "Fast point feature histograms (fpfh) for 3d registration," in *Proc. IEEE Intl. Conf. on Robot. and Automat.*, 2009, pp. 3212–3217.

- [46] S. Salti, F. Tombari, and L. Di Stefano, "Shot: Unique signatures of histograms for surface and texture description," *Comput. Vision and Image Understanding*, vol. 125, pp. 251–264, 2014.
- [47] M. Bosse and R. Zlot, "Place recognition using keypoint voting in large 3d lidar datasets," in *Proc. IEEE Intl. Conf. on Robot. and Automat.*, 2013, pp. 2677–2684.
- [48] S. Gupta, T. Guadagnino, B. Mersch, N. Trekel, M. V. Malladi, and C. Stachniss, "Efficiently closing loops in lidar-based slam using point cloud density maps," *arXiv preprint arXiv:2501.07399*, 2025.
- [49] E. Rublee, V. Rabaud, K. Konolige, and G. Bradski, "Orb: An efficient alternative to sift or surf," in *Proc. IEEE Intl. Conf. on Comput. Vision*, 2011, pp. 2564–2571.
- [50] Y. Zhang, Y. Tian, G. Yang, Z. Li, M. Luo, E. Li, and F. Jing, "Intensity triangle descriptor constructed from high-resolution spinning lidar intensity image for loop closure detection," *IEEE Robot. and Automat. Lett.*, 2024.
- [51] Y. Park, G. Pak, and E. Kim, "Re-trip: Reflectivity instance augmented triangle descriptor for 3d place recognition," pp. 2226–2232, 2025.
- [52] M. A. Uy and G. H. Lee, "Pointnetvlad: Deep point cloud based retrieval for large-scale place recognition," in *Proc. IEEE Conf. on Comput. Vision and Pattern Recog.*, 2018, pp. 4470–4479.
- [53] T.-X. Xu, Y.-C. Guo, Z. Li, G. Yu, Y.-K. Lai, and S.-H. Zhang, "Transloc3d: Point cloud based large-scale place recognition using adaptive receptive fields," *arXiv preprint arXiv:2105.11605*, 2021.
- [54] K. Vidanapathirana, M. Ramezani, P. Moghadam, S. C. Sridharan, and C. Fookes, "Logg3d-net: Locally guided global descriptor learning for 3d place recognition," in *Proc. IEEE Intl. Conf. on Robot. and Automat.*, 2022, pp. 2215–2221.
- [55] C. Choy, J. Gwak, and S. Savarese, "4d spatio-temporal convnets: Minkowski convolutional neural networks," in *Proc. IEEE Conf. on Comput. Vision and Pattern Recog.*, 2019, pp. 3075–3084.
- [56] J. Komorowski, "Improving point cloud based place recognition with ranking-based loss and large batch training," in *Proc. Intl. Conf. Pattern Recog.*, 2022, pp. 3699–3705.
- [57] E. Griffiths, M. Haghghat, S. Denman, C. Fookes, and M. Ramezani, "Hotformerloc: Hierarchical octree transformer for versatile lidar place recognition across ground and aerial views," in *Proc. IEEE Conf. on Comput. Vision and Pattern Recog.*, 2025, pp. 6648–6658.
- [58] Y. Shen, T. Tuna, M. Hutter, C. Cadena, and N. Zheng, "Forestlpr: Lidar place recognition in forests attentioning multiple bev density images," in *Proc. IEEE Conf. on Comput. Vision and Pattern Recog.*, 2025, pp. 6659–6669.
- [59] L. Luo, S.-Y. Cao, X. Li, J. Xu, R. Ai, Z. Yu, and X. Chen, "Bevplace++: Fast, robust, and lightweight lidar global localization for unmanned ground vehicles," *IEEE Trans. Robot.*, 2025.
- [60] L. Luo, S.-Y. Cao, B. Han, H.-L. Shen, and J. Li, "Bvmatch: Lidar-based place recognition using bird's-eye view images," *IEEE Robot. and Automat. Lett.*, vol. 6, no. 3, pp. 6076–6083, 2021.
- [61] M. Jung, L. F. T. Fu, M. Fallon, and A. Kim, "Imlpr: Image-based lidar place recognition using vision foundation models," *arXiv preprint arXiv:2505.18364*, 2025.
- [62] M. Oquab, T. Darcet, T. Moutakanni, H. V. Vo, M. Szafraniec, V. Khalidov, P. Fernandez, D. HAZIZA, F. Massa, A. El-Nouby *et al.*, "Dinov2: Learning robust visual features without supervision," *J. of Machine Learning Research*.
- [63] G. Pramatarov, D. De Martini, M. Gadd, and P. Newman, "Boxgraph: Semantic place recognition and pose estimation from 3d lidar," in *Proc. IEEE/RSJ Intl. Conf. on Intell. Robots and Sys.*, 2022, pp. 7004–7011.
- [64] W. Ma, H. Yin, P. J. Wong, D. Wang, Y. Sun, and Z. Su, "Tripletloc: One-shot global localization using semantic triplet in urban environments," *IEEE Robot. and Automat. Lett.*, 2024.
- [65] K. Vidanapathirana, P. Moghadam, S. C. Sridharan, and C. Fookes, "Spectral geometric verification: Re-ranking point cloud retrieval for metric localization," *IEEE Robot. and Automat. Lett.*, vol. 8, no. 5, pp. 2494–2501, 2023.
- [66] D. Cattaneo, M. Vaghi, and A. Valada, "Lcdnet: Deep loop closure detection and point cloud registration for lidar slam," *IEEE Trans. Robot.*, vol. 38, no. 4, pp. 2074–2093, 2022.
- [67] J. Komorowski, M. Wysoczanska, and T. Trzcinski, "Egonn: Egocentric neural network for point cloud based 6dof relocalization at the city scale," *IEEE Robot. and Automat. Lett.*, vol. 7, no. 2, pp. 722–729, 2021.
- [68] J.-F. Tremblay and M. Béland, "Towards operational marker-free registration of terrestrial lidar data in forests," *ISPRS J. Photogramm. Remote Sensing*, vol. 146, pp. 430–435, 2018.
- [69] Y. Liang, J. Liu, J. Lei, J. Muhojoki, A. Kukko, H. Kaartinen, J. Hyypää, D. Xu, and W. Zhang, "Ground-to-air collaborative lidar global localization in forest environments," *Expert Systems with Applications*, p. 131267, 2026.
- [70] W. Xu, Y. Cai, D. He, J. Lin, and F. Zhang, "Fast-lio2: Fast direct lidar-inertial odometry," *IEEE Trans. Robot.*, vol. 38, no. 4, pp. 2053–2073, 2022.
- [71] K. Chen, R. Nemiroff, and B. T. Lopez, "Direct lidar-inertial odometry: Lightweight lio with continuous-time motion correction," in *Proc. IEEE Intl. Conf. on Robot. and Automat.*, 2023, pp. 3983–3989.
- [72] Z. Qin, H. Yu, C. Wang, Y. Guo, Y. Peng, S. Ilic, D. Hu, and K. Xu, "Geotransformer: Fast and robust point cloud registration with geometric transformer," *IEEE Trans. Pattern Analysis and Machine Intell.*, vol. 45, no. 8, pp. 9806–9821, 2023.
- [73] M. Grupp, "evo: Python package for the evaluation of odometry and slam." <https://github.com/MichaelGrupp/evo>, 2017.
- [74] Y. Pan, T. Sun, L. Zhu, L. Nunes, I. Armeni, J. Behley, and C. Stachniss, "Register any point: Scaling 3d point cloud registration by flow matching," *arXiv preprint arXiv:2512.01850*, 2025.
- [75] D. Wisth, M. Camurri, and M. Fallon, "Vilens: Visual, inertial, lidar, and leg odometry for all-terrain legged robots," *IEEE Trans. Robot.*, vol. 39, no. 1, pp. 309–326, 2022.
- [76] A. Geiger, P. Lenz, C. Stiller, and R. Urtasun, "Vision meets robotics: The kitti dataset," *Intl. J. of Robot. Research*, vol. 32, no. 11, pp. 1231–1237, 2013.
- [77] W. Maddern, G. Pascoe, C. Linegar, and P. Newman, "1 year, 1000 km: The oxford robotcar dataset," *Intl. J. of Robot. Research*, vol. 36, no. 1, pp. 3–15, 2017.
- [78] S. Ao, Q. Hu, H. Wang, K. Xu, and Y. Guo, "Buffer: Balancing accuracy, efficiency, and generalizability in point cloud registration," in *Proc. IEEE Conf. on Comput. Vision and Pattern Recog.*, 2023, pp. 1255–1264.
- [79] M. Seo, H. Lim, K. Lee, L. Carlone, and J. Park, "Buffer-x: Towards zero-shot point cloud registration in diverse scenes," *arXiv preprint arXiv:2503.07940*, 2025.

Appendix

A. Ground Truth Generation for Evo25

To generate consistent ground truth trajectories for the nine sequences in `Evo25:00-08`, we first estimated local trajectories using VILENS [75] with LiDAR and IMU data. The sessions were then coarsely aligned based on common locations. To further refine this alignment, inter-session constraints were added at the point cloud level via robust pairwise frame matching using TEASER++ [20]. All TEASER++ matches were manually verified to ensure high alignment quality. Candidate frame pairs were selected via nearest neighbor matching across all possible session combinations. Finally, all local trajectories and inter-session constraints were jointly optimized using GTSAM to produce globally consistent multi-session trajectories.

B. Learning-based Methods with Training Datasets

We analyzed the impact of training data on learning-based baselines. Each learning-based method was evaluated under three training regimes: (1) urban, (2) in-domain forest, and (3) out-of-domain forest.

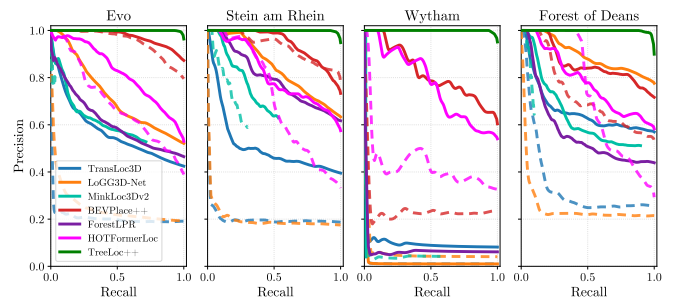
Urban vs. Forest: We analyzed the impact of training data on learning-based baselines by using urban datasets (KITTI [76] and Oxford RobotCar [77]) for training, and evaluating the models on the Oxford Forest Place Recognition Dataset. BEVPlace++ and LoGG3D-Net were trained on KITTI, while the other models used Oxford RobotCar. All models employed pretrained checkpoints, except for TransLoc3D. As shown in Table. 12, models trained on urban datasets exhibited limited generalization to forest environments. This trend is also reflected in Fig. 24a, where urban-trained models underperformed in terms of PR curves, with performance degrading across all sequences. In contrast, models trained on Wild-Places achieved moderate performance, particularly in structured scenes such as Stein am Rhein. While training on Wild-Places improved overall performance, their performance still remained limited across the evaluation sequences. This suggests two key insights: first, that models trained on urban datasets struggle to generalize to forest environments, even though such datasets are

TABLE 12: Comparative analysis of intra-session place recognition in Oxford Forest using urban-trained versus forest-trained models

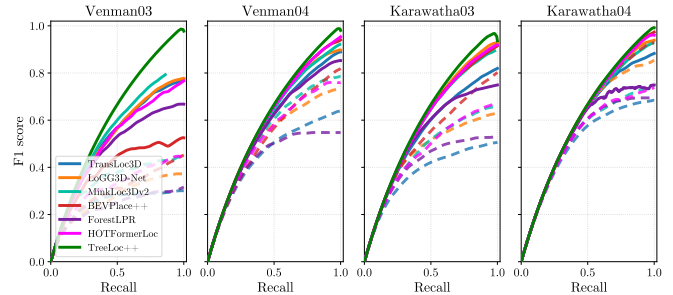
Dimension / Method	Stein am Rhein				Wytham				
	R@1	MR	MF1	AUC	R@1	MR	MF1	AUC	
Learning-based (Urban)	TransLoc3D	0.187	0.000	0.316	0.198	0.010	0.000	0.020	0.011
	LoGG3D-Net	0.175	0.002	0.298	0.197	0.041	0.000	0.078	0.044
	MinkLoc3Dv2	0.426	0.037	0.398	0.233	0.041	0.000	0.078	0.025
	BEVPlace++	0.727	0.375	0.865	0.941	0.235	0.000	0.383	0.220
	HOTFormerLoc	0.330	0.136	0.598	0.703	0.327	0.063	0.535	0.414
Learning-based (Forest)	TransLoc3D	0.395	0.004	0.566	0.507	0.082	0.000	0.151	0.091
	LoGG3D-Net	0.633	0.257	0.776	0.843	0.010	0.012	0.020	0.012
	MinkLoc3Dv2	0.538	0.086	0.577	0.429	0.031	0.010	0.020	0.006
	BEVPlace++	0.776	0.263	0.900	0.929	0.592	0.172	0.795	0.806
	HOTFormerLoc	0.570	0.107	0.768	0.811	0.541	0.113	0.718	0.756
Ours	TreeLoc++	0.941	0.937	0.986	0.998	0.796	0.962	0.994	0.993

TABLE 13: Comparative analysis of intra-session place recognition in Wild-Places using in-domain-trained versus out-of-domain forest-trained models

Dimension / Method	Venman04				Karawatha04				
	R@1	MR	MF1	AUC	R@1	MR	MF1	AUC	
Learning-based (Oxford Forest)	TransLoc3D	0.469	0.000	0.638	0.496	0.520	0.000	0.684	0.618
	LoGG3D-Net	0.584	0.042	0.737	0.745	0.745	0.332	0.854	0.921
	MinkLoc3Dv2	0.647	0.029	0.785	0.774	0.593	0.134	0.744	0.776
	BEVPlace++	0.694	0.015	0.819	0.666	0.860	0.088	0.929	0.951
	ForestLPR	0.188	0.000	0.317	0.181	0.377	0.037	0.548	0.554
	HOTFormerLoc	0.613	0.013	0.765	0.717	0.587	0.031	0.749	0.742
Learning-based (Wild-Places)	TransLoc3D	0.801	0.003	0.890	0.868	0.790	0.003	0.883	0.928
	LoGG3D-Net	0.814	0.113	0.898	0.934	0.885	0.012	0.939	0.945
	MinkLoc3Dv2	0.853	0.037	0.921	0.913	0.867	0.360	0.927	0.947
	BEVPlace++	0.885	0.234	0.940	0.964	0.945	0.617	0.975	0.987
	ForestLPR	0.743	0.045	0.853	0.839	0.599	0.271	0.749	0.865
	HOTFormerLoc	0.911	0.037	0.953	0.955	0.924	0.359	0.966	0.978
Ours	TreeLoc++	0.924	0.980	0.993	0.998	0.903	0.940	0.995	0.998



(a) Precision-Recall Curve in Oxford Forest Place Recognition Dataset



(b) F1-Recall Curve in Wild-Places

FIGURE 24: Precision-Recall and F1-Recall curves showing the impact of training domains. (Top) Urban-trained models (dashed) perform worse on Oxford Forest, compared to models trained on forest datasets (solid), indicating limited generalization to natural environments. (Bottom) Even across forest datasets, models trained on Oxford Forest (dashed) perform worse on Wild-Places, compared to those trained directly on Wild-Places (solid), highlighting challenges in cross-forest generalization.

large-scale and readily available, which limits their practical applicability; and second, that a domain gap persists even within forest environments, degrading performance across evaluation sequences. We further investigate this forest domain gap in the Wild-Places experiments.

In-domain vs. out-of-domain forest: We examined the effect of training data from different forest domains by comparing models trained on Wild-Places and the Oxford Forest Place Recognition Dataset, evaluated on Wild-Places sequences. As shown in Table. 13, methods trained on Oxford Forest showed a clear drop in performance, compa-

TABLE 14: Pose estimation performance comparison with registration methods.

Dimension / Method	Evo:Single									Venman03									
	1-4 m (N = 4670)			4-7 m (N = 4668)			7-10 m (N = 4669)			1-4 m (N = 4189)			4-7 m (N = 4481)			7-10 m (N = 4097)			
	SR	ATE	ARE	SR	ATE	ARE	SR	ATE	ARE	SR	ATE	ARE	SR	ATE	ARE	SR	ATE	ARE	
2D	Quatro (S)	0.948	0.108	0.269	0.856	0.161	0.446	0.794	0.198	0.623	0.547	0.311	0.239	0.551	0.309	0.259	0.458	0.291	0.359
	Quatro (L)	0.818	0.208	0.727	0.479	0.265	1.077	0.242	0.290	1.250	0.381	0.315	0.448	0.322	0.316	0.625	0.261	0.312	0.809
	Quatro (T)	0.881	0.164	0.199	0.745	0.199	0.314	0.698	0.212	0.365	0.848	0.163	0.408	0.836	0.170	0.437	0.706	0.183	0.521
	TEASER++ (S)	1.000	0.059	0.197	0.997	0.094	0.318	0.979	0.133	0.463	1.000	0.046	0.081	1.000	0.061	0.110	1.000	0.083	0.157
	TEASER++ (L)	0.848	0.223	0.844	0.506	0.278	1.263	0.247	0.296	1.306	0.815	0.262	0.562	0.620	0.290	0.694	0.433	0.299	0.862
	TEASER++ (T)	1.000	0.038	0.039	1.000	0.047	0.056	0.999	0.052	0.068	1.000	0.036	0.039	0.999	0.055	0.064	0.991	0.074	0.090
	KISS-Matcher (S)	0.997	0.079	0.306	0.970	0.128	0.531	0.861	0.172	0.731	1.000	0.082	0.179	0.999	0.114	0.268	0.974	0.158	0.391
	KISS-Matcher (L)	0.794	0.197	0.815	0.400	0.257	1.135	0.168	0.272	1.208	0.839	0.214	0.516	0.628	0.261	0.724	0.357	0.282	0.921
	TreeLoc++	1.000	0.017	0.039	1.000	0.025	0.054	0.998	0.031	0.068	1.000	0.027	0.042	0.991	0.046	0.071	0.967	0.067	0.105
3D	TEASER++ (S)	1.000	0.065	0.197	0.996	0.103	0.509	0.975	0.146	0.740	1.000	0.055	0.176	1.000	0.073	0.241	1.000	0.098	0.338
	TEASER++ (L)	0.833	0.236	1.277	0.468	0.298	1.936	0.199	0.322	2.297	0.778	0.290	0.871	0.555	0.324	1.126	0.357	0.340	1.446
	TEASER++ (T)	0.990	0.074	0.263	0.961	0.100	0.417	0.934	0.116	0.526	0.976	0.084	0.208	0.920	0.112	0.352	0.845	0.131	0.521
	KISS-Matcher (S)	0.995	0.090	0.718	0.958	0.148	1.092	0.815	0.198	1.405	1.000	0.100	0.467	0.997	0.137	0.661	0.962	0.188	0.879
	KISS-Matcher (L)	0.749	0.225	1.721	0.315	0.290	2.237	0.114	0.310	2.389	0.788	0.246	1.082	0.530	0.295	1.413	0.267	0.320	1.706
	TreeLoc++	0.990	0.061	0.261	0.960	0.090	0.418	0.930	0.112	0.531	0.976	0.080	0.211	0.910	0.110	0.360	0.824	0.143	0.544

S and L use small and large voxel sizes with PPFH-based correspondences, while T uses tree centers and base heights with initial all-to-all correspondences.

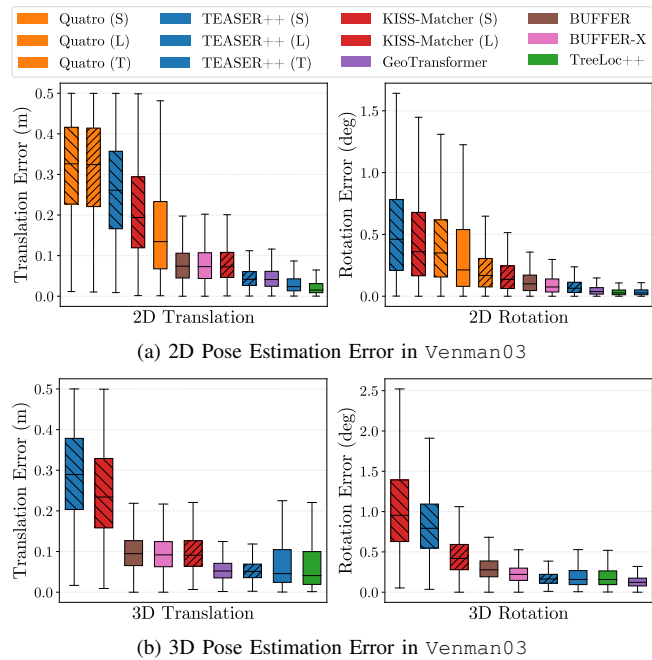


FIGURE 25: Box plots of pose errors on the `Evo:Single` for the 1 – 4 m interval. Boxes indicate the IQR, with the median marked inside. `TreeLoc++` consistently exhibits low median error and tight error distribution.

able to that of urban-trained models, despite both datasets being forest environments. Similarly, in Fig. 24b, methods trained on Oxford Forest consistently yielded lower F1 scores, indicating decreased retrieval quality. These results suggest that, even within the same broader domain, forest environments can differ substantially, making it difficult for learning-based methods to generalize. This highlights the potential of well-designed hand-crafted methods to provide more robust performance across diverse forest conditions. In particular, `TreeLoc++`, which achieves learning-comparable performance without training, emerges as a strong alternative to learning-based approaches in forest environments.

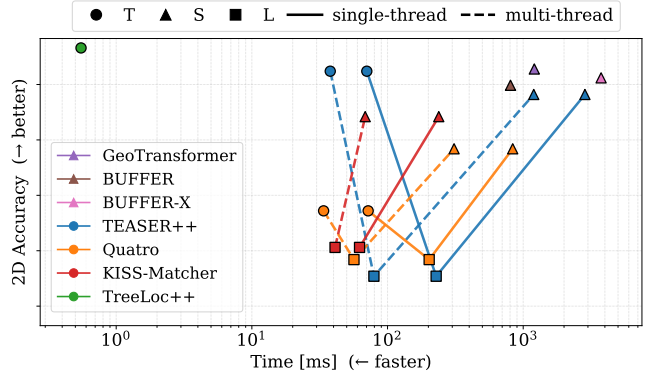


FIGURE 26: 2D pose estimation error with time consumption on the `Venman03` for the 1 – 4 m translation interval

C. Pose Estimation Benchmark: Registration Methods

Evaluation protocol: We evaluated `TreeLoc++` as a registration method against learning-based baselines (`GeoTransformer` [72], `BUFFER` [78], `BUFFER-X` [79]) and hand-crafted baselines (`Quatro` [21], `TEASER++` [20], `KISS-Matcher` [22]). To evaluate performance across spatial separations, we grouped query-candidate pairs into translation ranges of 1 – 4 m, 4 – 7 m, and 7 – 10 m. For each range, we selected two candidates per query from `TreeLoc++` retrieval outputs (one above and one below the midpoint) based on overlap ratio, without guaranteeing true positives. To avoid bias toward nearby candidates, we disabled the translation penalty $p(\|t\|)$ during candidate selection. Classical baselines were evaluated with two voxel resolutions, small (S) and large (L), as well as a tree-only setting (T) using stem centers and base heights. Voxel sizes were 0.5/1.0 m for `Evo:Single` and 1.0/2.0 m for `Venman03`. We also tested whether `TreeLoc++` tree-level features (stem centers and base heights) improve existing registration pipelines, and compared runtime to assess efficiency. Learning-based baselines were evaluated on the 1 – 4 m range using official configurations and pretrained checkpoints.

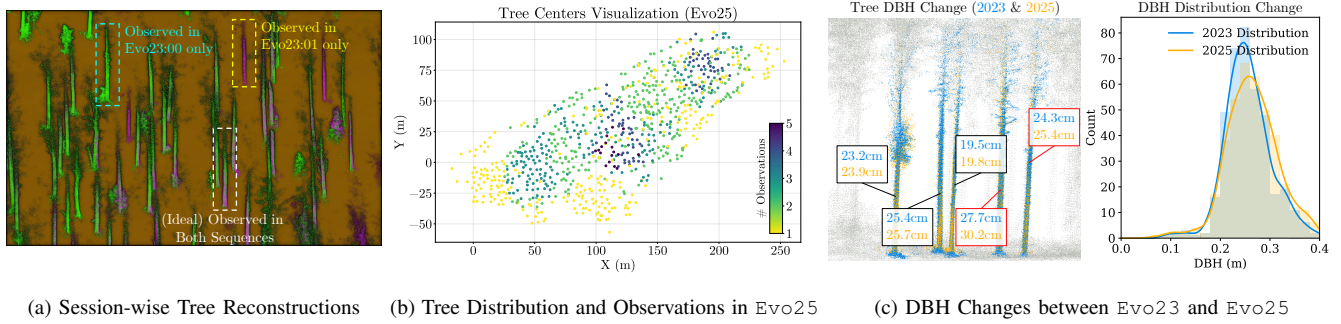


FIGURE 27: (a) Trees reconstructed by RealtimeTrees in Evo23:00–01. Different trajectories lead to session-specific observations, motivating inventory management for partially covered areas. (b) Tree-center distributions in Evo25 after TreeLoc++ alignment; brighter colors indicate lower observation rates, highlighting regions requiring additional exploration. (c) Tree point clouds and corresponding DBH measurements from 2023 and 2025 (left). Continuous ecological monitoring is enabled by tracking tree correspondences over time. The DBH distribution for trees in the 20–80% growth percentile range (right) shows a slight shift to the right.

TreeLoc++: As summarized in Table. 14, TreeLoc++ achieved the best overall 2D pose accuracy across all distance ranges. In the 1–4 m range, it significantly outperformed both classical and learning-based baselines in translation and rotation error, as visualized in Fig. 25a. In 3D, accuracy degraded with distance for all methods; nevertheless, TreeLoc++ maintained centimeter-level errors comparable to dense point cloud-based approaches. Fig. 25b shows increased interquartile range (IQR), but the medians remained low, supporting the effectiveness of TreeLoc++ for metric localization.

Tree-based vs. point-based registration: To evaluate the value of tree-level features, we compared TreeLoc++ with TEASER++ (T). They achieved comparable accuracy on sparse inputs, indicating that our matching strategy offers robustness similar to that of maximum-clique optimization. In contrast, classical point-based baselines were more sensitive: Quatro performed poorly due to restrictive orientation assumptions, TEASER++ required fine voxel resolutions to achieve high success, and KISS-Matcher offered an efficiency-accuracy trade-off.

These results further highlight a trade-off between sparse and dense representations. Specifically, dense point cloud-based methods (S) gain an advantage in 3D stability, as evidenced by their stable performance in Venman03, by utilizing ground points to provide comprehensive 6-DoF constraints. By comparison, tree-based methods can become unstable when tree centers and base points are degraded by limited visibility or long-range occlusion. In practice, TreeLoc++ mitigates this by using the translation penalty $p(\|t\|)$ during retrieval to favor closer candidates, where tree-level features are more distinctive, thereby improving robustness for metric localization.

Runtime: TreeLoc++ also provides a clear computational advantage by combining compact tree-level representations with retrieval-informed correspondences. As shown in Fig. 26, it completes full pose estimation in under 1 ms on a single CPU thread by reusing correspondences and avoiding expensive clique solving. In contrast, classical and learning-

based baselines typically require over 100 ms, and can exceed 1 s at small voxel sizes. This makes them impractical for real-time deployment despite their accuracy, whereas TreeLoc++ incurs minimal latency while maintaining high precision.

In summary, TreeLoc++ achieves accurate and efficient 2D localization, while delivering 3D localization performance competitive with point cloud-based registration methods at a substantially lower computational cost. Its comparable performance to TEASER++ (T) indicates that tree inventory features, when paired with precise matching, are sufficient for robust forest localization.

D. Multi-Session Digital Forest Inventory Maintenance

Problem setting: In this section, we demonstrate a practical DFI maintenance pipeline by updating tree traits across multiple sessions (Fig. 2) and illustrating how the updated inventory can be used in long-term forest monitoring. In practical forest deployments, robots cannot exhaustively explore all regions and instead revisit forests along a limited set of traversed paths, yielding uneven observation coverage over time. Consequently, reconstructions can be session-dependent: some trees are successfully reconstructed in one session but missed in another due to viewpoint, occlusion, or partial coverage, as illustrated in Fig. 27a. This motivates multi-session updates, where observations are fused across sessions to recover missing trees and refine tree-level attributes, maintaining a consistent inventory for the regions of interest.

Multi-session fusion: Building on the multi-session registration results, we establish tree correspondences across sessions by transforming inventories into a common global frame and associating them via spatial proximity and stem traits. Instead of re-running the reconstruction on aggregated clusters, we consolidate the per-session tree traits by adopting the attributes from the session with the minimum DBH for each unique tree. This approach is designed to mitigate the overestimation of DBH typically caused by alignment errors, such as odometry drift or sensor noise. This

TABLE 15: Localization performance under varying true-positive distance thresholds. Dataset-level N denotes the total number of queries, while threshold-level N indicates queries with at least one true-positive candidate within the given distance.

Dimension / Method	Evo:Single (Queries: $N = 2334$)									Karawatha04 (Queries: $N = 1547$)									
	3 m ($N_{TP} = 1138$)			5 m ($N_{TP} = 1361$)			10 m ($N_{TP} = 1715$)			3 m ($N_{TP} = 328$)			5 m ($N_{TP} = 328$)			10 m ($N_{TP} = 342$)			
	MF1	R@50	ATE	MF1	R@50	ATE	MF1	R@50	ATE	MF1	R@50	ATE	MF1	R@50	ATE	MF1	R@50	ATE	
2D	LoGG3D-Net	0.596	0.726	0.125	0.685	0.671	0.128	0.741	0.566	0.146	0.863	0.892	0.125	0.939	0.900	0.131	0.940	0.878	0.119
	MinkLoc3Dv2	0.537	0.040	0.324	0.640	0.035	0.310	0.702	0.026	0.297	0.813	0.087	0.327	0.928	0.088	0.283	0.979	0.073	0.305
	BEVPlace++	0.889	0.990	0.122	0.933	0.979	0.134	0.939	0.920	0.151	0.892	0.511	0.211	0.975	0.502	0.217	0.997	0.499	0.225
	RING++	0.268	0.538	0.217	0.223	0.555	0.222	0.182	0.467	0.225	0.839	0.461	0.266	0.834	0.453	0.266	0.841	0.434	0.272
	BTC	0.725	0.951	0.142	0.761	0.929	0.145	0.843	0.860	0.167	0.506	0.531	0.163	0.621	0.527	0.158	0.817	0.529	0.156
	MapClosure	0.475	0.940	0.145	0.528	0.935	0.167	0.555	0.923	0.196	0.821	0.643	0.145	0.875	0.638	0.147	0.965	0.636	0.160
	TreeLoc	0.904	1.000	0.022	0.955	0.998	0.024	0.981	0.993	0.028	0.690	0.656	0.049	0.816	0.654	0.055	0.922	0.644	0.055
	TreeLoc++	0.986	0.999	0.025	0.991	0.995	0.026	0.990	0.992	0.031	0.971	0.926	0.037	0.992	0.924	0.038	0.995	0.909	0.039
3D	LoGG3D-Net	0.596	0.704	0.144	0.685	0.645	0.151	0.741	0.539	0.171	0.863	0.889	0.152	0.939	0.891	0.157	0.940	0.872	0.148
	MinkLoc3Dv2	0.537	0.030	0.338	0.640	0.026	0.334	0.702	0.019	0.307	0.813	0.028	0.302	0.928	0.046	0.327	0.979	0.018	0.298
	BTC	0.725	0.684	0.177	0.761	0.632	0.185	0.843	0.546	0.206	0.506	0.408	0.227	0.621	0.403	0.227	0.817	0.400	0.237
	MapClosure	0.475	0.916	0.154	0.528	0.897	0.177	0.555	0.881	0.207	0.821	0.640	0.145	0.875	0.635	0.148	0.965	0.632	0.160
	TreeLoc	0.904	0.976	0.089	0.955	0.967	0.095	0.981	0.939	0.107	0.690	0.594	0.128	0.816	0.593	0.135	0.922	0.583	0.144
	TreeLoc++	0.986	0.992	0.070	0.991	0.982	0.073	0.990	0.955	0.080	0.971	0.919	0.061	0.992	0.924	0.068	0.995	0.909	0.074

unified inventory ensures more robust tree-level attributes for consistent downstream analyses.

Observation-aware map consistency: The updated multi-session DFI integrates observations across sessions into a consistent stem map, enabled by TreeLoc++’s robust global alignment and tree association. Fig. 27b shows the spatial distribution of stem centers and the number of sessions in which each tree was reconstructed. Trees in frequently revisited areas appear across multiple sessions, whereas those near the map boundaries are reconstructed in fewer sessions. This spatial pattern qualitatively indicates successful consolidation of observations in well-covered regions, while also revealing under-observed areas that may require further exploration.

Temporal analysis using tree-level attributes: Fig. 27c illustrates the potential for long-term ecological monitoring by comparing tree-level attributes across sessions. Using TreeLoc++, we identify consistent tree correspondences between $Evo23$ and $Evo25$, enabling reliable tracking of individual trees over time. However, detecting DBH changes over a two-year interval is challenging, as actual biological growth is limited. Furthermore, LiDAR sensor noise, such as the 3 cm accuracy of the Hesai XT64 used in $Evo25$, introduces measurement variability. Consequently, some trees in Fig. 27c (left, red boxes) show DBH variations exceeding the typical growth rate of 2 – 4 mm per year. Nevertheless, the DBH distribution for the 20-80% percentile range (Fig. 27c, right) exhibits a slight rightward shift consistent with long-term growth. This morphological stability allows TreeLoc++ to leverage trees as reliable long-term landmarks, supporting robust global localization and consistent ecological monitoring across sessions.

E. Ablation Study on Positive Threshold Selection

Evaluation Protocol: We assess how localization performance varies with different true positive thresholds by evaluating MF1, R@50, and ATE. We consider three thresh-

olds: 3 m (as used in Wild-Places), 10 m (from the Oxford Forest Place Recognition dataset), and 5 m as a middle ground adopted in this manuscript. As in previous experiments, LoGG3D-Net and MinkLoc3Dv2 employ feature-based matching and RANSAC-based registration, without re-ranking.

Performance Trends: As shown in Table. 15, most methods exhibit increased MF1 as the threshold grows, while R@50 and ATE tend to degrade. This behavior is expected, as larger thresholds admit more distant candidates as true positives, increasing recall and thus MF1. However, this also reduces geometric overlap between matched pairs, leading to less reliable correspondences and increased translation error. This trend is consistent across both 2D and 3D localization.

Stability across Thresholds: TreeLoc++ maintains strong performance across all thresholds and is the only method that consistently achieves centimeter-level ATE. In contrast, most baseline methods show large variations in MF1 and R@50 as the threshold changes, indicating a strong dependence on the threshold and reduced robustness to the definition of true positives. This variation indicates that the similarity scoring and correspondence selection mechanisms do not reliably capture real-world spatial relationships, leading to exaggerated sensitivity to threshold values and reduced stability in localization performance.

Conclusion: These findings highlight that TreeLoc++ delivers consistent and robust localization performance across a wide range of true positive thresholds, in contrast to baseline methods that are highly sensitive to threshold selection. This stability underscores its suitability for real-world deployment, where fixed thresholds may not always be well defined.